

## Non-Isolated Integrated Motor Drive and Battery Charger Based on the Split-Phase PM Motor for Plug-in Vehicles

*Master of Science Thesis in Electric Power Engineering*

**Isabel Serrano Guillén**

**Álvaro Bermejo Fernández**

Department of Energy and Environment  
Division of Electric Power Engineering  
CHALMERS UNIVERSITY OF TECHNOLOGY  
Göteborg, Sweden, 2013



Non-Isolated Integrated Motor Drive and Battery Charger  
Based on the Split-Phase PM Motor for Plug-in Vehicles

By

Isabel Serrano Guillén

Álvaro Bermejo Fernández

**Supervisor**

Saeid Haghbin

**Examiner**

Ola Carlson

Department of Energy and Environment

*Division of Electric Power Engineering*

CHALMERS UNIVERSITY OF TECHNOLOGY

Göteborg, Sweden, 2013

NON-ISOLATED INTEGRATED MOTOR DRIVE AND BATTERY CHARGER BASED  
ON THE SPLIT-PHASE PM MOTOR FOR PLUG-IN VEHICLES

ISABEL SERRANO GUILLÉN

ÁLVARO BERMEJO FERNÁNDEZ

© ISABEL SERRANO GUILLÉN, 2013

© ÁLVARO BERMEJO FERNÁNDEZ, 2013

Department of Energy and Environment

Division of Electric Power Engineering

CHALMERS UNIVERSITY OF TECHNOLOGY

SE-412 96 Göteborg

Sweden

Telephone: + 46 (0)31-772 1000

Göteborg, 2013



# Non-Isolated Integrated Motor Drive and Battery Charger Based on the Split-Phase PM Motor for Plug-in Vehicles

ISABEL SERRANO GUILLÉN

ÁLVARO BERMEJO FERNÁNDEZ

Department of Energy and Environment

Division of Electric Power Engineering

Chalmers University of Technology

## ABSTRACT

In electric vehicles and plug-in hybrid electric vehicles, the utility grid charges the vehicle battery through a battery charger. Different solutions have been proposed to reduce the size and cost of the charger. One solution to achieve this is to include the devices used in the traction circuit in the charger circuit; this is called an integrated motor drive and battery charger.

A split-phase PM motor, a motor with double set of windings, gives the opportunity to implement different winding configurations to keep the motor at stand-still when it is connected to the grid. The motor will act as inductors in the charging process. This is an advantageous chance in order to use the motor in an integrated battery charger. In the current thesis, a non-isolated battery charger based on some of these special configurations is tested.

Two different PM motors are utilized in proposed chargers. Different windings configurations have been practically tested. The main challenge is to keep the motor in stand-still during charge operation. Practical results show that with proposed schemes, the motors are in stand-still.

A National Instrument CompactRIO system is used to perform the control of the integrated charger in the practical implementation. A brief explanation of the practical setup and a user guide for running the experimental system is included as well.

**Keywords: Plug-in vehicles, battery charger, integrated charger, split-phase PM motor, Pulse Width Modulation (PWM), CompactRIO controller.**

## ACKNOWLEDGEMENTS

First of all we would like to offer our sincerest gratitude to our supervisor Saeid Haghbin, for giving us the chance to be part of this interesting project. His availability and support have been a great help during all the work in the division. Also we are really grateful to him for giving us the opportunity of contributes with our work in international publications.

Thanks also to Ola Carlson, for giving us the opportunity to do this Master Thesis work in the Electric Power Engineering Division of Chalmers University of Technology. The division has provided us all the equipment which we have needed for completing our thesis.

Thanks also to all the team that takes part of the division who have given us their kind support and availability making our time in the department enjoyable and pleasant. Furthermore, we would like to thank to our room colleagues who have made our daily work atmosphere friendly.

Finally, thanks to our families for making possible this experience in Sweden, and our friends who were supporting us during all our work.

*Isabel Serrano Guillén and Álvaro Bermejo Fernández*

*Göteborg, Sweden*

*2013*

# NOMENCLATURES

PM	Permanent magnet
IPM	Interior permanent magnet
PHEV	Plug-in hybrid electric vehicles
EV	Electric vehicles
$d$	Direct axis
$q$	Quadrature axis
$V_{DC}$	DC Bus voltage
$V_{LL}$	Line to line voltage
EMF	Electromotive force
PI	Proportional integral
THD	Total harmonic distortion
$\psi_d$	Flux direct axis
$\psi_q$	Flux quadrature axis
$\psi_{pm}$	Permanent magnet flux
$L_{xy}$	Inductance of xy
$\omega$	Frequency
$i_d$	Current direct axis
$i_q$	Current quadrature axis
P	Number of poles
$T_e$	Electromagnetic torque
R	Resistance
L	Inductance
s	second
A	Ampere
V	Volts
W	Watt
$K_{pv}$	Voltage controller proportional coefficient
$K_{iv}$	Voltage controller integrator coefficient
$K_{ii}$	Current controller integrator coefficient
$K_{pi}$	Current controller proportional coefficient
$f_{sw}$	Switching frequency
VOC	Voltage Oriented Control
IGBT	Insulated gate bipolar transistor
PWM	Pulse Width Modulation
cRIO	CompactRIO control device

## LIST OF FIGURES

Figure 2.1: A typical electrical traction circuit in vehicle application.	4
Figure 2.2: Main diagram of a non-isolated integrated charger inside the vehicle.	4
Figure 2.3: Simple diagram of the proposed integrated charger in charging mode.	5
Figure 2.4: Electrical charger circuit in the proposal integrated battery charger.	6
Figure 2.5: Diagram of the voltage oriented control schema used in the thesis.	7
Figure 2.6: Decoupled controller block diagram used in the control stage of the three-phase Boost rectifier.	8
Figure 3.1. Non isolated battery charger based on the dual-winding PM motor.	9
Figure 3.2. Cross-section of the split-phase PM motor with six stator winding.	10
Figure 3.3: Geometry of the 2 kW PM motor.	11
Figure 3.4: Winding configuration for the 2 kW PM motor: a) Serial connection, b) parallel connection configuration 1, c) parallel connection configuration 2.	13
Figure 3.5: Geometry of the 20 kW PM motor.	14
Figure 3.6: Winding configuration for the 20 kW PM motor: a) Serial connection, b) parallel connection.	15
Figure 4.1: Configuration used in the experimental setup for 2 kW PM motor.	17
Figure 4.2: Configuration used in the experimental setup for 20 kW PM motor.	17
Figure 4.3: Schema of the structure of the experimental setup tested.	18
Figure 4.4: Experimental setup using the 2 kW PM motor.	18
Figure 4.5: Voltage supply and extra inductances.	19
Figure 4.6: Measurement box containing the voltage and current transducers.	20
Figure 4.7: DC sources and relays box.	20
Figure 4.8: Inverter.	21
Figure 4.9: Potentiometer used in the battery role.	22
Figure 4.10: CRIO 9022 controller with the used modules.	22
Figure 4.11: Labview front panel interface used for the control.	23
Figure 4.12: Schema of digital PWM generation in the FPGA.	24
Figure 4.13: Current and voltage in the DC side for the tested charging time (2 kW motor).	25
Figure 4.14: Three phase currents during charging time (2 kW motor).	26
Figure 4.15: Current and voltage of phase A during charging time (2 kW motor).	26
Figure 4.16: Current and voltage over the windings during the charging time (2 kW motor).	27
Figure 4.17: Response of phase A current against a step of the DC voltage reference (2 kW machine).	27
Figure 4.18: Experimental setup using the 20 kW PM motor.	28

Figure 4.19: Current and voltage in the DC side for the tested charging time (20 kW motor).	30
Figure 4.20: Three phase currents during charging time (20 kW motor).	30
Figure 4.21: Current and voltage of phase A during charging time (20 kW motor).	31
Figure 4.22: Current and voltage over the windings during the charging time (20 kW motor).	31
Figure 4.23: Phase-shift between current and voltage during charging time (20 KW motor).	32
Figure 4.24: Response of phase A current against a step of the DC voltage reference (20 kW machine).	32
Figure A.1: Main screen of MAX.	40
Figure A.2: CompactRIO set in safe mode.	40
Figure A.3: Main screen of MAX when the CompactRIO software is fully installed.	41
Figure A.4: How to add the new CompactRIO in the project.	42
Figure A.5: Discovering the CompactRIO device in LabVIEW.	43
Figure A.6: View of the project explorer after move the files.	44
Figure A.7: Names for the inputs and outputs in CompactRIO modules.	45
Figure A.8: How to change the initial direction for the digital module used.	46
Figure A.9: View of the front panel when the system is running properly.	47
Figure B.1: Experimental setup for the inductance measurement.	49
Figure B.2: Serial winding connection for 2 kW PM motor.	50
Figure B.3: First parallel winding connection for 2 kW PM motor.	51
Figure B.4: Voltages and current in the measurement setup of the first parallel winding connection.	51
Figure B.5: Second parallel winding connection for 2 kW PM motor.	52
Figure B.6: Voltages and current in the measurement setup of the second parallel winding connection.	53
Figure B.7: Diagram of the practical setup for testing a non-isolated integrated charger.	54
Figure B.8: Practical setup performed for 20 kW PM motor.	54
Figure B.9: Serial winding connection for 20 kW PM motor.	55
Figure B.10: Parallel winding connection for 20 kW PM motor.	55
Figure B.11: Voltages and current in the experimental setup for the parallel winding connection.	57
Figure B.12: Simulation of the integrated charger system studied.	58
Figure B.13: Simulation results of the integrated charger system studied.	58
Figure B.14: Practical setup for measuring the leak inductance in the transformer.	59
Figure B.15: Practical setup for measuring the leak inductance in the autotransformer.	60
Figure B.16: Practical setup for measuring the leak inductance in the autotransformer+transformer.	60

## LIST OF TABLES

Table 3.1: Parameters of the 2 kW PM motor.	12
Table 3.2: Experimental results for the 2 kW PM motor.	12
Table 3.3: Parameters of the 20 kW PM motor.	14
Table 3.4: Experimental results for the 20 kW PM motor.	15
Table 4.1: Parameters of the inverter.	21

# TABLE OF CONTENTS

ABSTRACT .....	vii
ACKNOWLEDGEMENTS .....	viii
NOMENCLATURES.....	ix
LIST OF FIGURES.....	x
LIST OF TABLES .....	xii
TABLE OF CONTENTS .....	xiii
Chapter 1. Introduction .....	1
1.1. Background and Previous Work .....	1
1.2. Purpose and Contributions of the Thesis .....	1
1.3. Thesis Outline .....	1
Chapter 2. Integrated Motor Drives and Battery Chargers .....	3
2.1 Proposed non-isolated integrated charger .....	4
2.2 Circuit topology of the battery charger (PWM Boost rectifier) .....	5
2.3 Battery charger control.....	6
Chapter 3. Split-phase PM Motor .....	9
3.1. 2 kW PM motor.....	11
3.2. 20 kW PM motor.....	14
Chapter 4. Practical Implementation of Non-isolated Battery Charger .....	17
4.1. Main structure of the experimental setup.....	18
4.1.1. Voltage supply and extra inductances .....	19
4.1.2. Measurement box of voltage and current transducers .....	19
4.1.3. Auxiliary power supplies and relay .....	20
4.1.4. Inverter.....	21
4.1.5. Load (Role of battery) .....	21
4.1.6. CompactRIO Controller .....	22
4.1.7. Control implementation.....	23
4.1.7.1. FPGA block.....	23
4.1.7.2. Processor block .....	24
4.2. Results from the experimental setup .....	24
4.2.1. Integrated charger based on a 2 kW Split-Phase PM motor .....	24
4.2.2. Integrated charger based on a 20 kW Split-Phase PM motor.....	28

4.2.3. Discussions, limitations and improvements .....	33
Chapter 5. Conclusions and Future Work.....	35
5.1. Conclusions .....	35
5.2. Future work .....	35
References.....	37
Appendix A: User Guide for the Developed Software of the Non-isolated Battery Charger..	39
A.1. Software installation in the computer.....	39
A.2. CompactRIO installation.....	40
A.3. Adding the new compactRIO controller to the LabVIEW project.....	42
A.4. Deploying the VIs .....	43
A.5. Renaming the modules .....	45
A.6. Compiling the FPGA file .....	46
A.7. Running the system .....	47
A.8. Changing system parameters.....	47
Appendix B. Experimental Setup for the Motor Parameters Measurement .....	49
B.1. 2 kW PM motor .....	49
B.1.1. Serial Connection .....	50
B.1.2. Parallel Connection: first configuration .....	50
B.1.3. Parallel Connection: second configuration.....	52
B.2. 20 kW PM motor .....	53
B.2.1. Serial Connection .....	54
B.2.2. Parallel Connection .....	55
B.3. Leakage Inductances .....	59
B.3.1. Transformer .....	59
B.3.2. Autotransformer .....	60
B.3.3. Autotransformer + Transformer .....	60
Appendix C: Hardware Datasheets .....	63
CompactRIO controller .....	63
CompactRIO analog input module NI 9215. ....	65
CompactRIO digital input/output module NI 9401. ....	67
Isolation amplifier for the voltage transducers.....	69
LEM Current transducer.....	73
Semistack Semikron inverter .....	75

# Chapter 1. Introduction

---

This chapter describes the project background, the objective and the main structure of the thesis.

## 1.1. Background and Previous Work

Nowadays electric vehicles (EVs) and plug-in hybrid electric vehicles (PHEV) are developed by many companies. Since one of the most important challenge is the battery, many research and studies are performing to improve its characteristics.

The reduction of the cost, space and weight of battery charger is one of the most important aims. To achieve that, the proposal is using the hardware used during the traction mode, the motor and the inverter, in the charge time. That is called an integrated motor drive and battery charger. In this integrated charger, the motor is used as some inductors. As a drive system, a split phase PM motor with a double set of windings is used. The winding configuration changes from charging to traction operation mode through a relay device [1].

## 1.2. Purpose and Contributions of the Thesis

The main purpose of this thesis is to practically verify an integrated motor drive and non-isolated battery charger based on different winding configurations [1]. The contributions can be summarized as:

- Test of the control through two experimental setups with different PM motors and winding configurations, proving the suitability as a battery charger.
- Enhance the system control, programmed in Labview and implemented in a CompactRio controller in order to perform an efficient control over the battery charger.
- S. Haghbin, I. Serrano Guillén, “Integrated motor drive and non-isolated battery charger based on the torque cancellation in the motor,” *IEEE International Conference on Power Electronics and Drive Systems*, 2013.
- S. Haghbin, R. Ghorbani, A. Bermejo Fernández, I. Serrano Guillén, “An Integrated Motor Drive and Battery Fast Charger Station for Plug-in Vehicles,” *XIII Spanish-Portuguese Conference on Electrical Engineering(XIII CHLIE)*, 2013.

## 1.3. Thesis Outline

This thesis is divided into five chapters. After this introduction, Chapter 2 gives an explanation of integrated motor drives and battery chargers, describing the configurations and the proposals. Chapter 3 explains the characteristics of the split-phase motor and the PM

motors used in the experimental setup. The whole experimental setup, divided into different parts and the results obtained, are shown in Chapter 4. The conclusions and the future work proposed are in Chapter 5.

In addition, there are three appendixes. Appendix A is dedicated to a user guide of the CompactRIO controller, Appendix B explains the experimental setup used for measuring the parameters in the PM motors used and Appendix C recollects all the datasheet of the components used.

# Chapter 2. Integrated Motor Drives and Battery Chargers

---

Electric vehicles (EVs) and plug-in hybrid electric vehicles (PHEVs) use grid power to charge the battery while the vehicle is parked. Normally the traction circuit components are not engaged during the battery charging, so there is a possibility to use them in the charger circuit to reduce the system volume, weight, and cost. That is called an integrated motor drive and battery charger or simply an integrated charger in this context [1].

Generally there are two types of battery chargers: on-board type and stand-alone (off-board) type. Moreover, these battery chargers can be galvanically isolated or non-isolated from the utility grid, a detailed comparison between different kinds of battery chargers used in charger for vehicle applications currently used can be found in [1].

Recalling the related standards, galvanic isolation is not a mandatory requirement, but it can greatly ease the safety requirements. So, the isolation is a very favorable option if the cost and space can be afforded, interesting examples with probed efficiency can be found in [1].

Anyway, a non-isolated charger usually represents high cost solutions, due to the need of devices that provide some kind of isolation to the system, like an isolated transformer by example shown in [1]. When the implementation of an isolated battery charger is not possible, for cost or space reasons, a non-isolated charger become the most attractive solution. This kind of integrated chargers results more efficient than the non-isolated ones mainly because of the components, for instance in an integrated non-isolated charger there is not a need for an isolated transformer.

In this thesis, a non-isolated integrated battery charger based in a PM split-phase motor is explained and tested. The main idea of the integrated battery charger is to take advantage of the devices uses in the traction mode, and use them for charging operation. Based on this idea, the inverter used in the traction circuit showed in Fig. 2.1 will be used like a PWM controlled rectifier with a control strategy explained in the following sections. Since the controlled rectifier could be seen like the main component of the charging system, in the purposed integrated charger the motor used for the traction system is also used in the charger stage, the motor will represent an inductor. In Fig. 2.2 it can be observed the diagram of the proposed integrated charger include in a vehicle (the inverter will be connected to the grid through the motor in the charging stage).

The main problem of connecting the inverter through the motor in the charger stage is the developed torque in the motor because of the current flowing in the windings. The motor may start to rotate or vibrate if the developed torque is not controlled in a proper way. So, keep the motor in state of zero-torque operation is one important criterion in an integrated charger. For example, one solution for torque control is to use a mechanical brake to keep the rotor at stand-still, but if the motor starts to rotate, there will be induced back EMF that makes the control very complicated in addition to the imposed extra rotational losses [1].

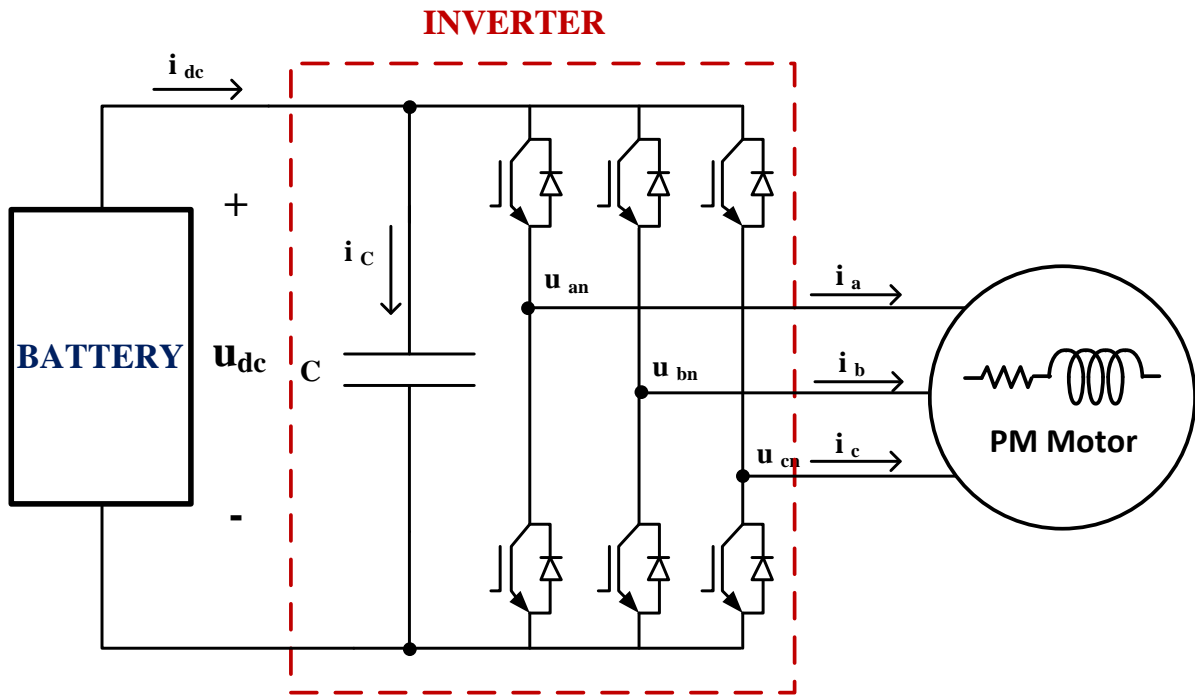


Figure 2.1: A typical electrical traction circuit in vehicle application.

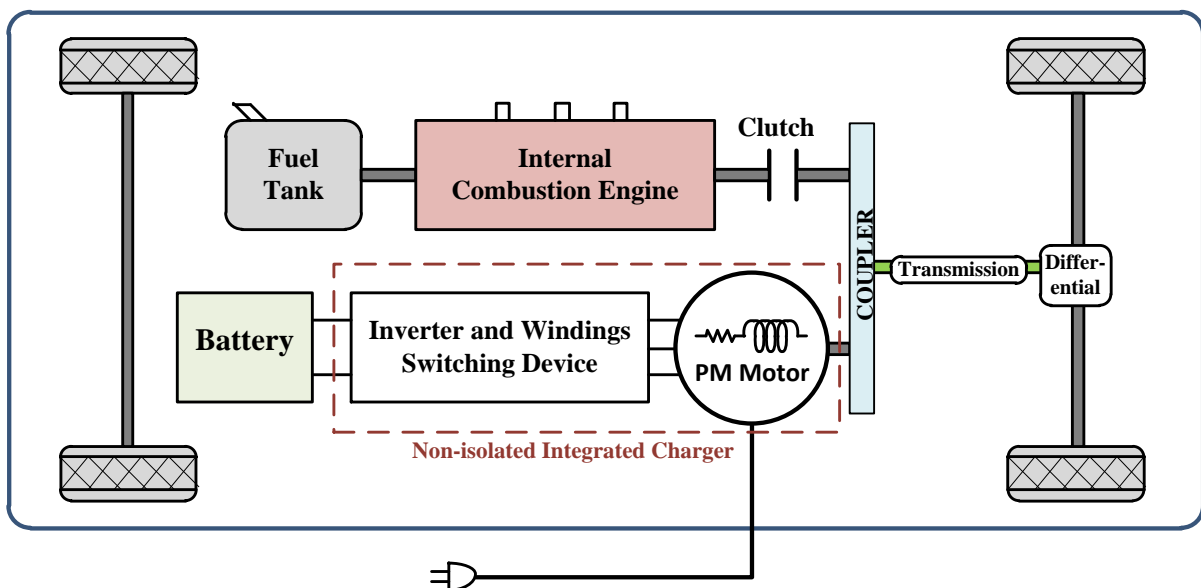


Figure 2.2: Main diagram of a non-isolated integrated charger inside the vehicle.

## 2.1 Proposed non-isolated integrated charger

To avoid any rotation in the rotor during the charging stage, the charger proposed in [1] is based on a special winding configuration for a split-phase PM motor that imposes zero-torque

condition and keeps the rotor in stand-still during the charging time. Detailed explanations of the configuration and the behavior of the PM motor during charging time are given in Chapter 3.

With these special winding reconfigurations, the machine will represent just an inductance and a resistance between the grid and the inverter, as is shown in Fig. 2.3. The inverter acting like a controlled three-phase Boost rectifier will be explained in the following sections.

Fig. 2.3 shows a simple diagram of the system in charging mode, where the inverter acts like a PWM controlled rectifier. It is possible to control the DC voltage in the battery side; therefore the power transmitted to the battery can be controlled through the control of the inverter. As mentioned earlier, the PM motor has a special winding configuration that keeps the motor at stand-still during the process.

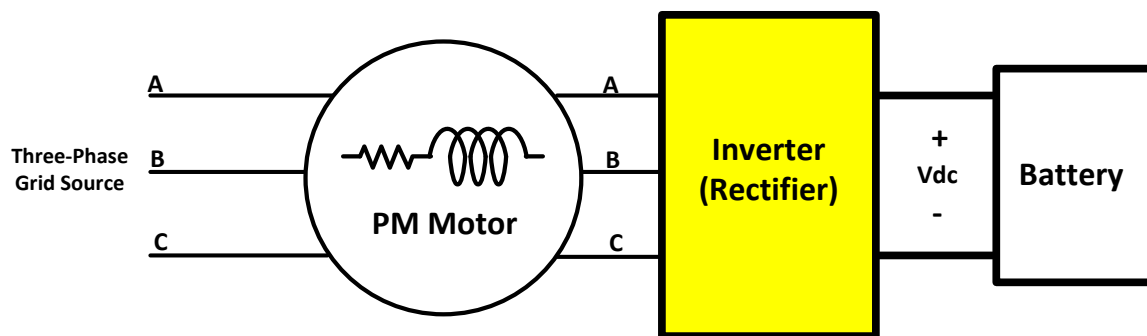


Figure 2.3: Simple diagram of the proposed integrated charger in charging mode.

## 2.2 Circuit topology of the battery charger (PWM Boost rectifier)

As is explained in the previous section, the inverter used in the traction mode in the vehicle will be used during the charging as a PWM controlled rectifier. Since the voltage level of the battery should be high (normally from 200 to 600 Vdc) in order to have proper operation in traction mode, a topology of Boost controlled rectifier will be used in charging mode. Fig. 2.4 shows the Boost converter power stage for the battery charger. To have a proper control in a Boost converter topology, the voltage in the DC should be higher than the peak line to line voltage of the input.

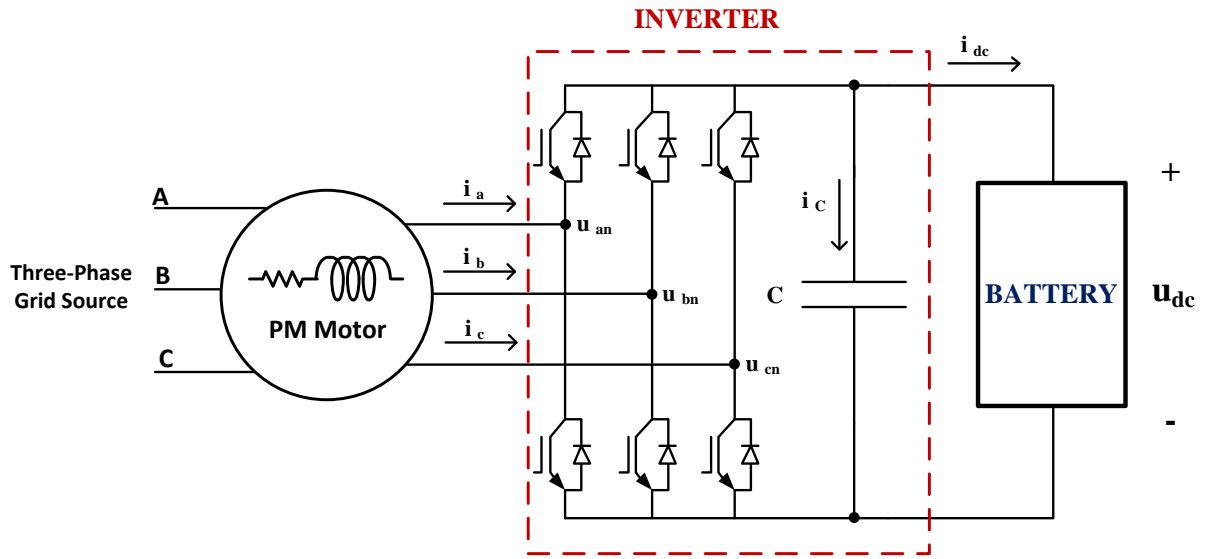


Figure 2.4: Electrical charger circuit in the proposal integrated battery charger.

### 2.3 Battery charger control

There are different ways to control a three-phase Boost converter [2]. For the control of the PWM Boost rectifier used in the developed integrated charger, the voltage-oriented control (VOC) method is used. VOC represents a high-efficiency method for the control stage in controlled rectifiers. A deep analysis of the method and its efficacy is reported in [3].

VOC is based on a series of transformation from a three phase stationary reference system  $abc$  to a synchronous rotating reference system  $dq$ , through a two phase stationary system  $\alpha\beta$ .

The first transformation is the change from the  $abc$  frame to the  $\alpha\beta$  frame, that is called Clarke transformation, which is based in the following equation:

$$\begin{bmatrix} \alpha \\ \beta \end{bmatrix} = \begin{bmatrix} \frac{2}{3} & -\frac{1}{3} & -\frac{1}{3} \\ 0 & \frac{1}{\sqrt{3}} & -\frac{1}{\sqrt{3}} \end{bmatrix} \begin{bmatrix} a \\ b \\ c \end{bmatrix}. \quad (2.1)$$

In the  $\alpha\beta$  reference frame, the degree of freedom is two ( $\alpha$  and  $\beta$ ) instead of three ( $a$ ,  $b$  and  $c$ ). But in the  $\alpha\beta$  frame the variables are still rotating, so another transformation should be performed in order to keep the variables constant for controlling at steady state; this transformation is called Park transformation that more information can be found in [3].

With the application of the Park transformation to the  $\alpha\beta$  values, the magnitudes in the dq frame remain constant at steady state and become DC values simplifying the control process. Fig. 2.5 shows the main diagram of the system including the dq control.

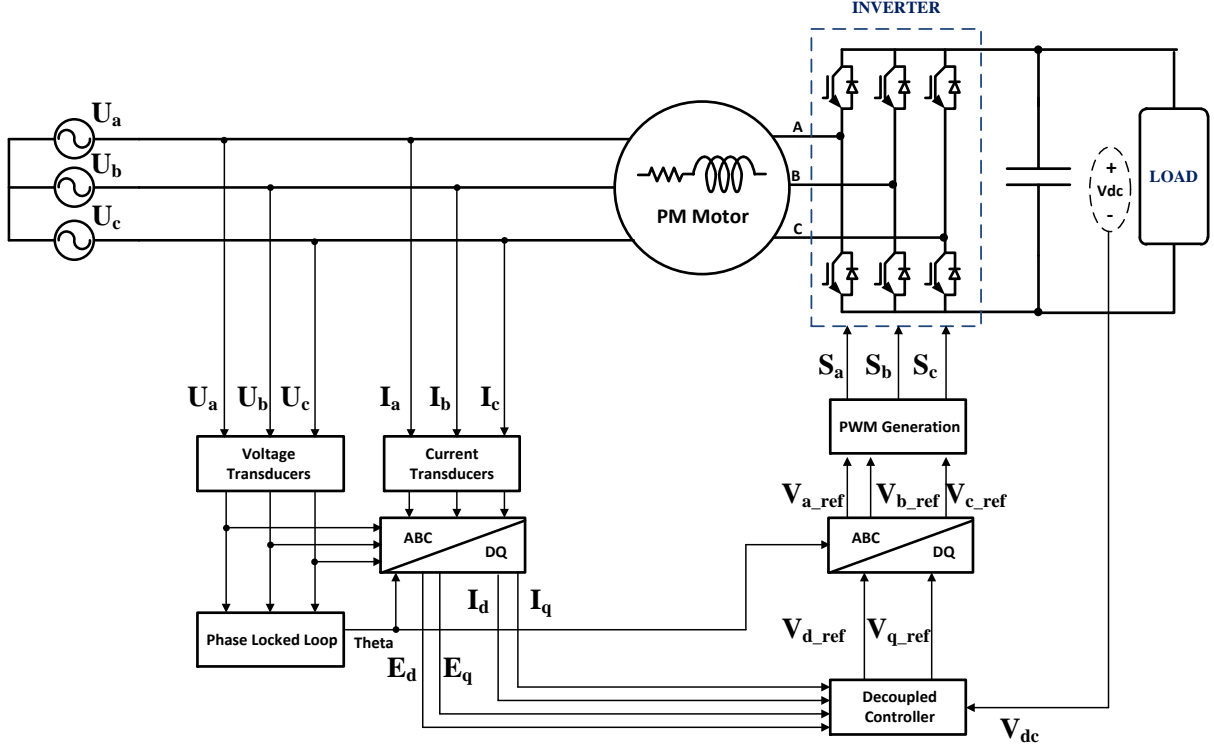


Figure 2.5: Diagram of the voltage oriented control schema used in the thesis.

Applying the explained transformations to rectifier the equations, the equations are referred to the dq reference as follows; the theoretical process used for obtaining the following equations can be found in [2]:

$$u_{Ld} = R_m i_{Ld} + L_m \frac{d}{dt} i_{Ld} - \omega L i_{Ld} + u_{Id} \quad (2.3)$$

$$u_{Lq} = R_m i_{Lq} + L_m \frac{d}{dt} i_{Lq} + \omega L i_{Lq} + u_{Iq} \quad (2.4)$$

where  $u_{Ld}$ ,  $u_{Lq}$ ,  $u_{Id}$  and  $u_{Iq}$  are line and inverter dq voltage components respectively,  $R_m$  and  $L_m$  represent the resistance and inductance of the PM motor, and  $\omega$  represents the frequency of the grid.  $i_{Ld}$  and  $i_{Lq}$  represents the dq components of the grid currents as well.

The power equations are described as:

$$P = \frac{3}{2} (u_{Ld} i_{Ld} + u_{Lq} i_{Lq}) \quad (2.5)$$

$$Q = \frac{3}{2}(u_{Lq}i_{Ld} - u_{Ld}i_{Lq}). \quad (2.6)$$

In this particular case, as a consequence of the transformation to the dq axes, the q component of the voltage and current should be zero. The power equations will be simplified as follows:

$$P = \frac{3}{2}u_{Ld}i_{Ld} \quad (2.7)$$

$$Q = 0. \quad (2.8)$$

As can be seen in above equations, as a result of  $i_{Lq} = 0$ , the equations will be simplified, keeping the reactive power in zero (unity power factor), and setting the active power in a function of  $i_{Ld}$ , since  $u_{Ld}$  represents the transformation of the source voltage that will be a fixed constant for the system.

To carry out the control a decoupled strategy is used as is shown in Fig. 2.6, that has a high performance [3].

Fig. 2.6 shows the main diagram of the decoupled control. As shown in Fig. 2.6, the error signal of the DC voltage goes inside the PI voltage controller that generates the  $i_d$  reference. The  $i_q$  reference is set in zero for keeping the unity power factor. Afterward, the shown decoupled strategy is used for generating the  $V_d$  and  $V_q$  for the inverter that will be transformed in a PWM block in order to generate the pattern for the inverter switches.

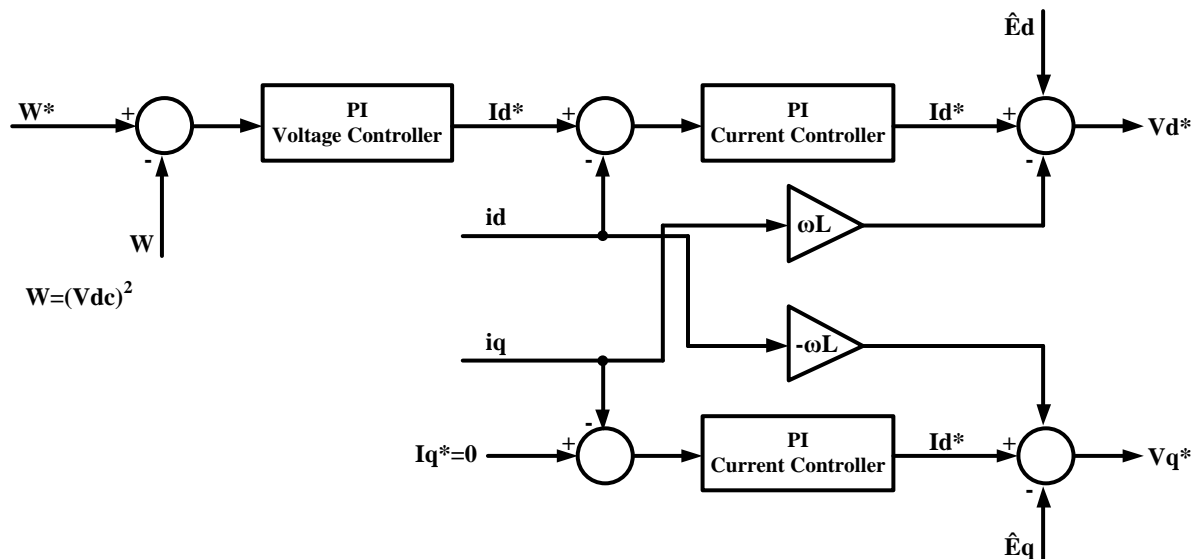


Figure 2.6: Decoupled controller block diagram used in the control stage of the three-phase Boost rectifier.

# Chapter 3. Split-phase PM Motor

A split-phase motor has double set of shifted three phase windings. They are used in different applications. Each winding of a split-phase motor is divided into two equivalent parts and shifted symmetrically around the stator geometry [4]. The current thesis studies the implications of using this motor in integrated chargers for electric vehicles and plug-in hybrid electric vehicles.

One important aspect of using the motor in the charger is that, due to the windings harmonic contents and the phase inductances dependent to the variable rotor position, there will be a current limitation that reduces the maximum charging power. That will be solved reducing the charge power for reaching an acceptable performance in the battery charging [4].

As is explained in the previous chapter, the condition of keeping the motor in stand-still during the charge time is one of the most important challenges for the proposed integrated battery charger. Different solutions to develop zero torque are studied. One of them uses a split-phase PM motor with dual inverters [5] and other solution is to use the split-phase PM motor as inductors and through the midpoints of the winding reach the zero torque condition since during the charge time the winding configuration used makes it possible to cancel out the mutual flux for using the leakage inductance in the battery charger [1].

Fig 3.1 shows how the winding configuration for a PM motor in traction and charging mode, that can be reconfigured through a switching device is [1].

In order to have the motor in stand-still and study its behaviour in an experimental setup, some variants for the winding configurations in a split-phase PM motor will be explained, tested and measured in the current chapter.

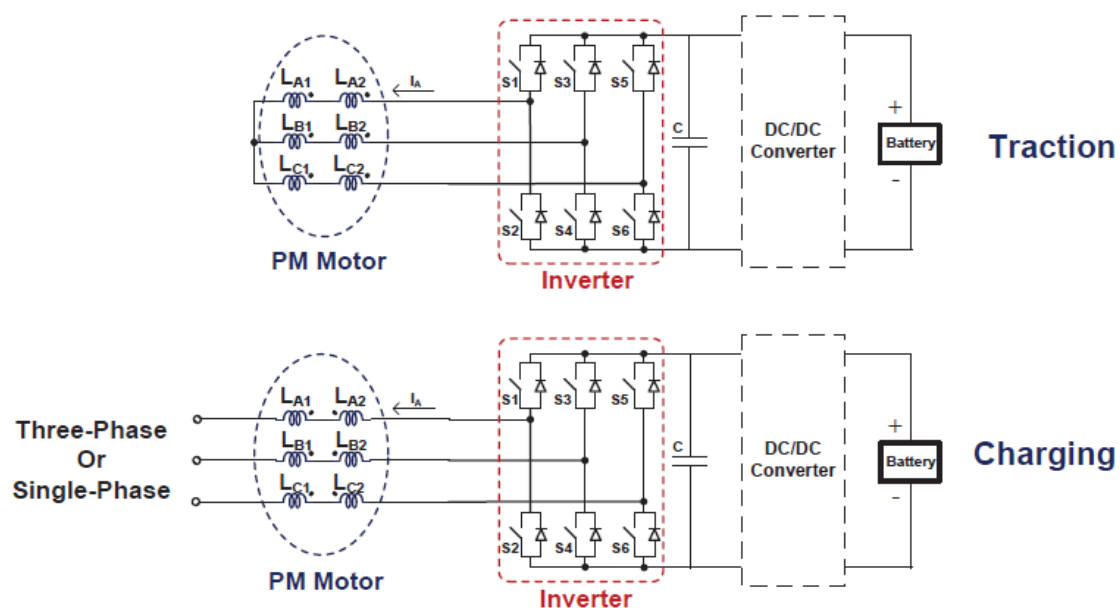


Figure 3.1: Non isolated battery charger based on the dual-winding PM motor [1].

Fig. 3.2 shows a cross-section of a two-pole PM motor, in which there are six winding shifted 30 electrical degrees. A model of this machine is studied and the mathematical equations are developed [6].

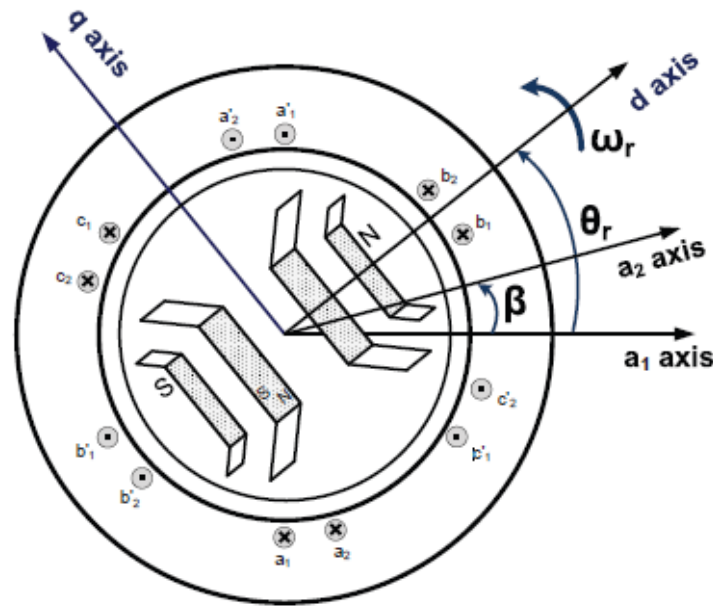


Figure 3.2: Cross-section of the split-phase PM motor with six stator winding [1].

For a split-phase machine the dynamic model of the electrical part can be expressed as [1]:

$$v_{d1} = r_s i_{d1} + \frac{d}{dt} \psi_{d1} - \omega_r \psi_{q1} \quad (3.1)$$

$$v_{q1} = r_s i_{q1} + \frac{d}{dt} \psi_{q1} + \omega_r \psi_{d1} \quad (3.2)$$

$$v_{d2} = r_s i_{d2} + \frac{d}{dt} \psi_{d2} - \omega_r \psi_{q2} \quad (3.3)$$

$$v_{q2} = r_s i_{q2} + \frac{d}{dt} \psi_{q2} + \omega_r \psi_{d2} \quad (3.4)$$

$$\psi_{d1} = L_d i_{d1} + L_{md} i_{d2} + \psi_{pm} \quad (3.5)$$

$$\psi_{q1} = L_q i_{q1} + L_{mq} i_{q2} \quad (3.6)$$

$$\psi_{d2} = L_{md} i_{d1} + L_d i_{d2} + \psi_{pm} \quad (3.7)$$

$$\psi_{q2} = L_{mq} i_{q1} + L_q i_{q2} \quad (3.8)$$

where  $L_d$ ,  $L_q$ ,  $L_{md}$ ,  $L_{mq}$ ,  $\psi_d$ ,  $\psi_q$  are the direct and quadrature axis winding self, mutual inductances and the fluxes, respectively. Moreover,  $L_d = L_l + L_{md}$  and  $L_q = L_l + L_{mq}$ . It is assumed that the zero components are zero due to symmetrical three-phase quantities.

The resultant electromagnetic torque can be described as [1]:

$$T_e = \frac{3P}{2} [\psi_{pm}(i_{q1} + i_{q2}) + (L_d - L_q)(i_{d1}i_{q1} + i_{d1}i_{q2} + i_{d2}i_{q1} + i_{d2}i_{q2})]. \quad (3.9)$$

For a PM motor  $L_d = L_q$  so the torque can be simplified to:

$$T_e = \frac{3P}{2} \psi_{pm}(i_{q1} + i_{q2}). \quad (3.10)$$

In [7] a more general case of a split-phase PM is presented. From (3.10) different configuration will be developed for the motor winding to achieve the condition of zero torque.

Two PM motors are studied in this thesis, one 2 kW and one 20 kW. The description of the motors and the configurations of their inductances are explained in this chapter.

### 3.1. 2 kW PM motor

A 6 pole permanent magnet motor with split stator is tested. The model of the PM motor is SBK5-0430 from BEVI Company. The rated speed of the machine is 1000 rpm. Fig. 3.3 shows an approximate geometry of the machine.

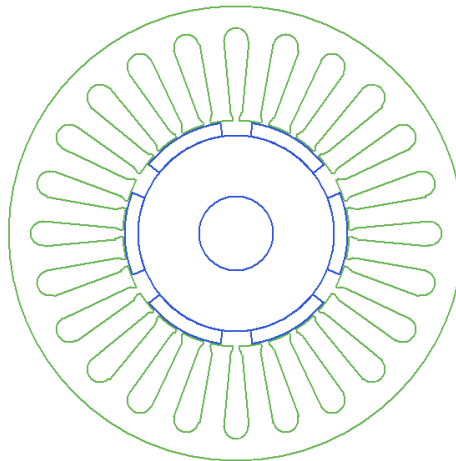


Figure 3.3: Geometry of the 2 kW PM motor.

Different configurations of the motor winding are studied; serial and parallel connection. These configurations are chosen to achieve zero torque in the machine for cancelling out of the mutual flux that as is developed in equation (3.10) creates zero electromagnetic torque. The experimental setup and the inductance measurements are presented in appendix B.

The parameters of the motor are shown in Table 3.1.

*Table 3.1: Parameters of the 2 kW PM motor.*

	Value	Units
Number of phases	3	-
Number of poles	6	-
Number of slots	24	-
Outer stator diameter	120	mm
Total axial length	101	mm
Rotor outer diameter	59	mm
Shaft diameter	20	mm
Air-gap height	0.5	mm
Rated torque	3.9	Nm
Rated speed	1000	r/min

The values obtained for the resistance and inductance in both cases are:

*Table 3.2: Experimental results for the 2 kW PM motor.*

	Equivalent Resistance	Equivalent Inductance
Serial connection	$R = 14,31 \Omega$	$L = 19,33 \text{ mH}$
Parallel connection conf. 1	$R = 3,5775 \Omega$	$L = 4,64 \text{ mH}$
Parallel connection conf. 2	$R = 0,3975 \Omega$	$L = 1,357 \text{ mH}$

The criterion chosen for selecting the winding configuration of the PM motor is the highest value of the equivalent inductance, due to a high inductance reduces the ripple of the current and it makes easier the control. In addition, in parallel winding connection the motor can handle the double current in each phase than in serial connection. For these reasons, the configuration used in the experimental setup is the first parallel winding connection.

Fig. 3.4 shows the different configurations tested. In this PM motor, since the stator windings are not shifted, the value of the equivalent inductance does not change depending of the rotor position. This is an important point for the implementation of the control.

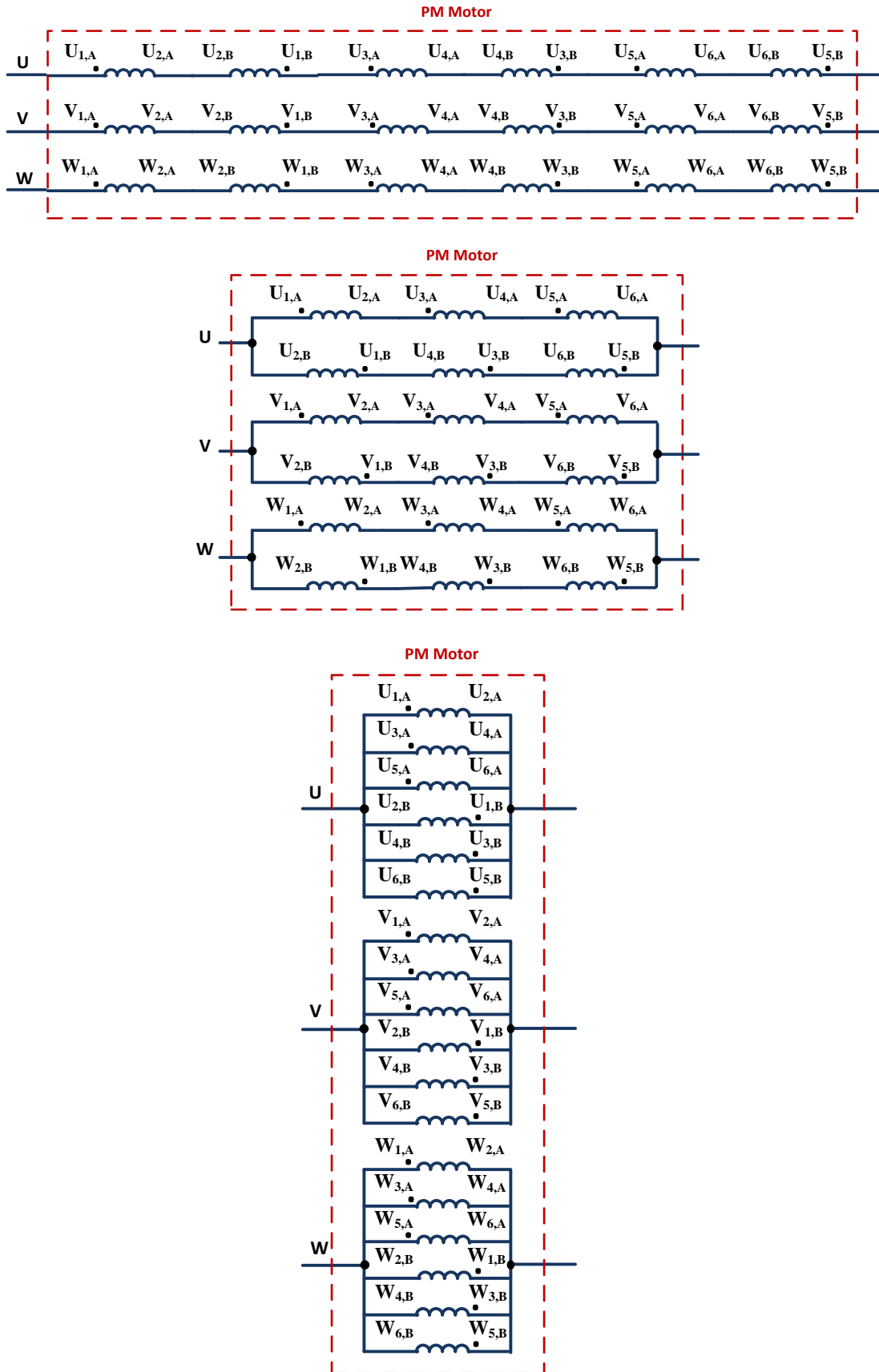


Figure 3.4: Winding configuration for the 2 kW PM motor: a) Serial connection, b) parallel connection configuration 1, c) parallel connection configuration 2.

### 3.2. 20 kW PM motor

A 4 pole interior permanent magnet (IPM) motor is studied in this section. This machine was designed as an innovative integrated charger able to use the traction drive system in an inverted power direction scheme [8]. For that aim the machine is constructed for working in conditions of traction and charge mode, since the windings can be reconfigured depending of the desired operation mode. The geometry of the machine is shown in Fig. 3.5. The interior permanent magnet motor can work at a maximum speed of 6500 rpm, with a rated speed of 1500 rpm. An important characteristic of this motor are the shifted stator windings.

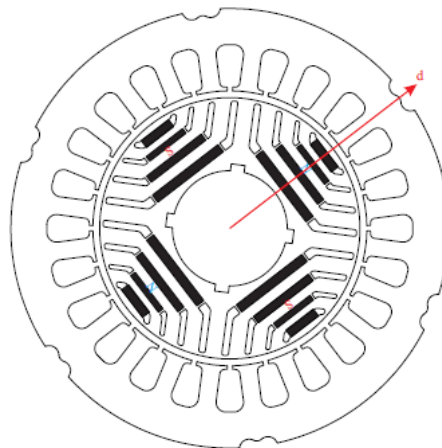


Figure 3.5: Geometry of the 20 kW PM motor [10].

The 20 kW PM motor used was designed by Kashif Khan [8]. The geometry of the machine is, initially, designed to maximize the reluctance torque and after magnets are introduced to increase it. In Table 3.3, the main characteristics of the 20 kW PM motor are summarized.

In the same way to the 2 kW PM motor, different configurations are studied for the machine fulfilling the condition of zero torque due to the cancelling out between them. The results obtained in the measurement are shown in Table 3.4.

Table 3.3: Parameters of the 20 kW PM motor.

	Value	Units
Number of phases	3	-
Number of poles	4	-
Number of slots	24	-
Outer stator diameter	180	mm
Total axial length	330	mm
Rotor outer diameter	112	mm
Shaft diameter	51	mm
Air-gap height	0.35	mm
Rated torque	127	Nm
Rated speed	1500	r/min

Table 3.4: Experimental results for the 20 kW PM motor.

	Equivalent Resistance	Equivalent Inductance
Serial connection	$R = 1.6 \Omega$	$L = 8.8 \text{ mH}$
Parallel connection	$R = 0.4 \Omega$	$L = 6.6 \text{ mH}$

Fig. 3.6 show the configurations tested. For the same reasons that are mentioned for the case of 2 kW PM motor, in parallel connection the motor can handle the double current in each phase and the value of the inductance is the highest making the control easier, the parallel configuration is chosen for the experimental setup.

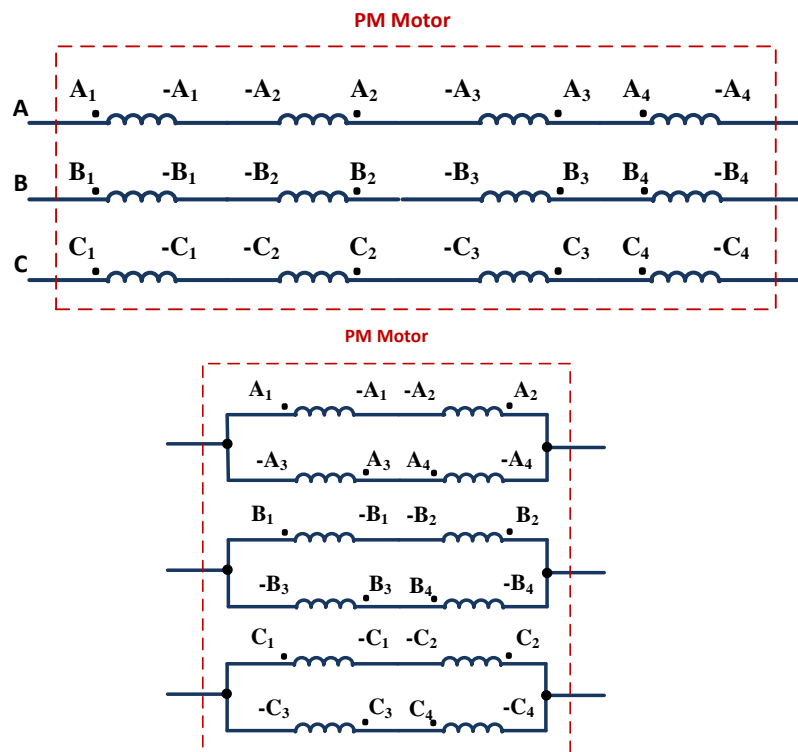


Figure 3.6: Winding configuration for the 20 kW PM motor: a) Serial connection, b) parallel connection.

As mentioned before, the windings in the stator of the 20 kW PM motor are shifted which make the value of the inductance a function of the rotor position. For this reason it is not possible have an accurate value for the inductance of the motor and it will affect in the control stage at the time of setting the parameters for the controller.

Another important issue observed in the 20 kW IPM is that, when the inductance value of the configurations were measured, the motor could not be fed with high voltages which generate high currents, due to the motor started to shake and producing a considerably noise. More information about this phenomenon can be found in [1].



# Chapter 4. Practical Implementation of Non-isolated Battery Charger

In order to probe the reliability of the non-isolated charger with the configuration of the split-phase PM motor explained before, two experimental setups are implemented and tested in the lab.

The first implemented setup uses the 2 kW PM motor with the parallel configuration explained in the previous chapter and is shown in Fig. 4.1. With this configuration the developed torque for the machine in these conditions is close to zero. This conditions leads in a zero speed (the machine remains in stand-still) during the charging time.

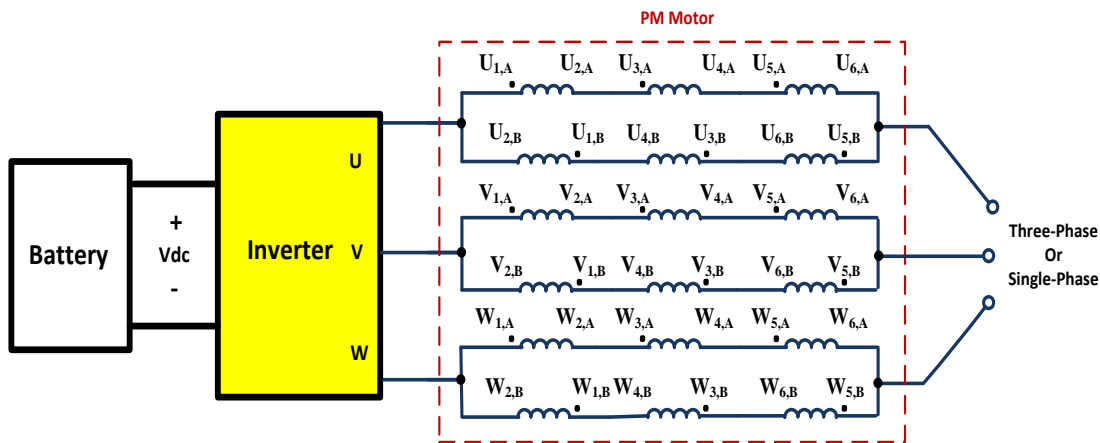


Figure 4.1: Configuration used in the experimental setup for 2 kW PM motor.

In the second setup, the 20 kW PM motor, described on Chapter 3, is used. The winding configuration is shown in Fig. 4.2, and like in the previous case, with this configuration the rotor maintained the requirement of zero torque during the charging time.

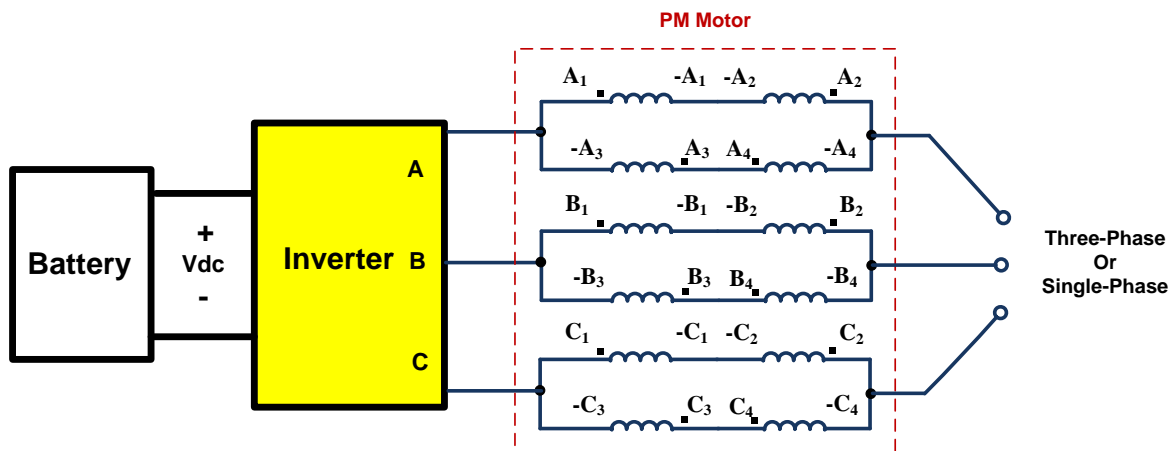


Figure 4.2: Configuration used in the experimental setup for 20 kW PM motor.

#### 4.1. Main structure of the experimental setup

Fig. 4.3 shows the main structure of the experimental setups, the main part of the system are the motor, the inverter, the relays (relay box), measurement interfaces (measurement box), the controller, and the load that perform the role of the battery. Fig. 4.4 shows the real setup.

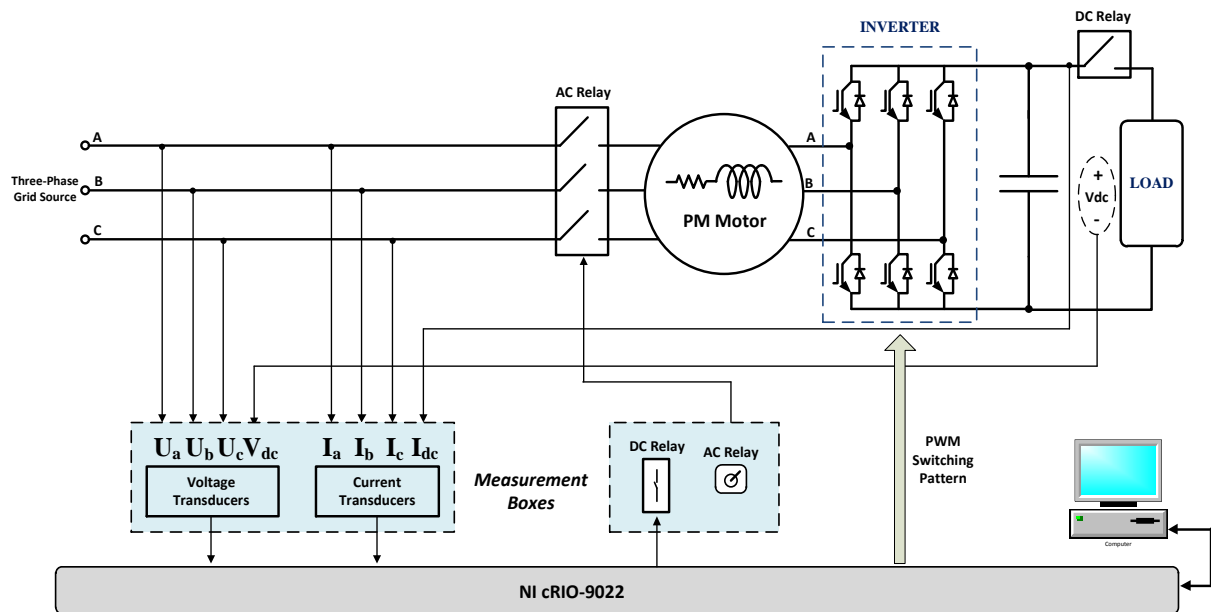


Figure 4.3: Schema of the structure of the experimental setup tested.

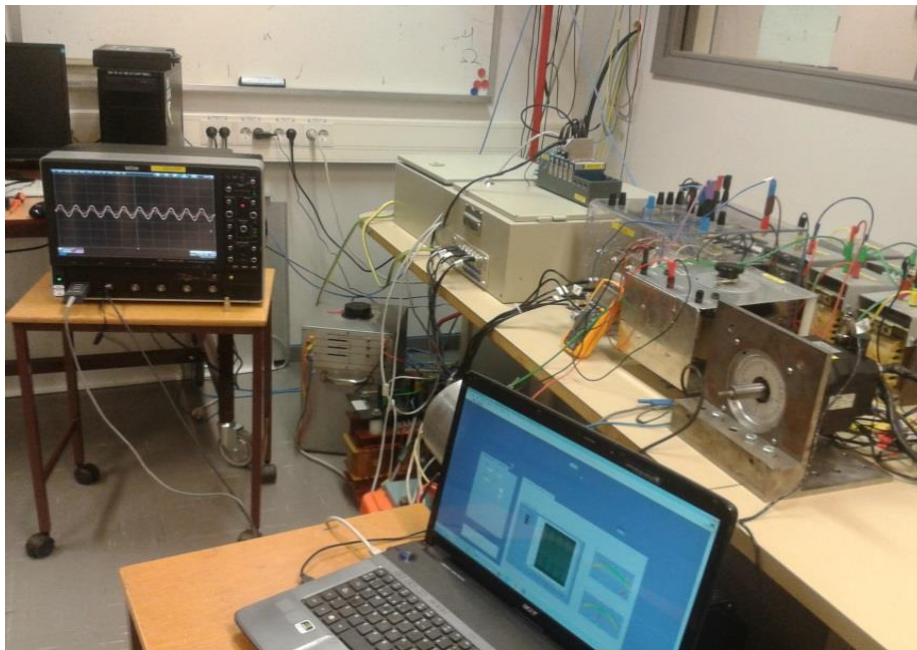
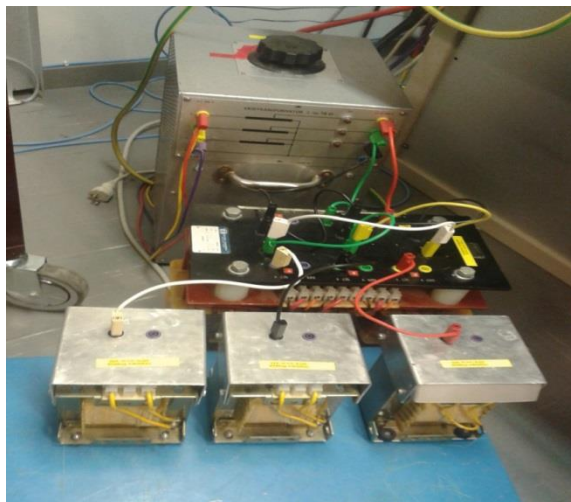


Figure 4.4: Experimental setup using the 2 kW PM motor.

### 4.1.1. Voltage supply and extra inductances

Since the measurement box cannot handle very high level of currents and voltages, the grid voltage should be reduced through the use of an autotransformer and a transformer that provide galvanic isolation from the grid as shows Fig. 4.5. This setup also allows modifying the voltage level to probe the behavior of the system against different input voltages.



*Figure 4.5: Voltage supply and extra inductances.*

The leak inductance of the supply system (transformer + autotransformer) had to be measured in order to calculate the parameters for the control stage. An inductance of 4.23 mH is measured (explanation of the measurements are given in Appendix B).

Due to some difficulties in the control stage, an extra inductance had to be added to the system, these inductances reduce the current ripple and make the system easier to control. The value of the used extra inductance is 20 mH.

### 4.1.2. Measurement box of voltage and current transducers

As is explained in Chapter 2, voltages and currents from AC side and DC side should be known in order to perform the control of the Boost converter (role of the inverter in the battery charger system).

In order to measure the voltages, four voltage transducers UMAT2 have been used; three are used to measure the voltage of each AC phase, and the other one is used to measure the DC voltage. The function of these transducers is reducing the measured voltage by a resistive divider; the transducers reduce the voltage from a range of  $\pm 400$  V to a  $\pm 10$  V signal that can be set like an input for the CompactRIO controller.

For the currents measurement, four LEM LA 50-S/SP1 are used. This device with galvanic isolation between the primary and the secondary circuit provides a proportional current in the output to the measured current in the input. This secondary is equipped with a resistor to make sure that the signal that is being used as an input of CompactRIO controller is always kept in the range of  $\pm 10V$ . The configuration can be observed in Fig. 4.6.

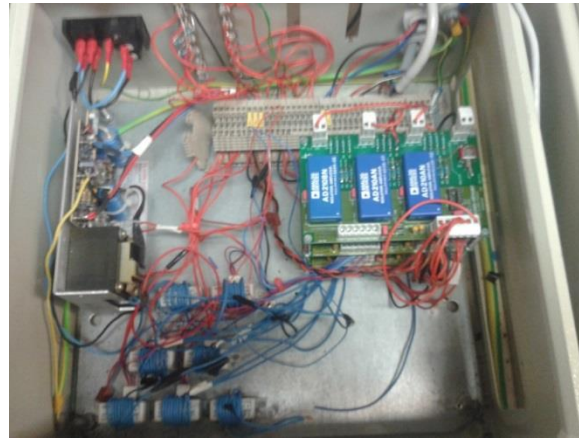


*Figure 4.6: Measurement box containing the voltage and current transducers.*

### 4.1.3. Auxiliary power supplies and relay

The different transducers of the measurement box and the inverter need to be fed with a source. To fulfill this purpose a box with two power supplies (one for the inverter and one for the measurement transducers) is used in the setup.

In this box are also located the relays for connecting the system to the grid as well as a relay for connecting or disconnecting the DC load. The AC relay is controllable with a physical switch in the box and the DC relay is activated through a digital signal from the CompactRIO controller. Fig. 4.7 shows all the elements.



*Figure 4.7: DC sources and relays box.*

#### 4.1.4. Inverter

A 4-leg Semikron inverter AN-800 is used in the experimental setup. Since the inverter has four legs available and for the control system only three are needed, one of the legs remains unused. Fig. 4.8, shows the inverter.

Detailed information about the inverter can be found in Table 4.1.

*Table 4.1: Parameters of the inverter.*

Parameter	Value	Description
$V_{dc}$	0-750	Input DC Voltage
$I_n[A_{rms}]$	30	Rated rms current per phase
$I_{ma}[A]$	40	Max. Current
$P_{max}$	30000	Max. Output power

In order to reduce the current ripple to an acceptable value and to perform an efficient control, the inverter switching frequency is carried out by PWM pulses generated by the FPGA of the CompactRIO controller, with a switching frequency of 10 kHz.

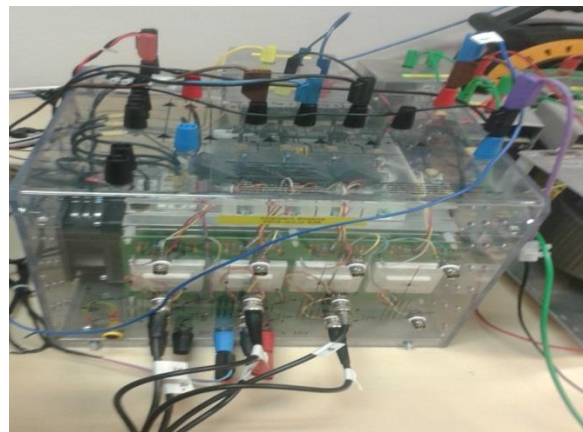


*Figure 4.8: Inverter.*

#### 4.1.5. Load (Role of battery)

In the system, a potentiometer with regularly load is used taking the role of the battery. The load value is set to 50 Ohms. It is adjusted to 95% of its total value as is shown in Fig. 4.9.



Figure 4.9: Potentiometer used in the battery role.

#### 4.1.6. CompactRIO Controller

The control is carried out by CompactRIO 9022, a real time controller from National Instruments. The controller mainly consists of two parts.

The first part consists of an embedded controller, based in a 500 MHz processor used for performing the most complex operations and a FPGA with a 40 MHz internal clock used for performing the fastest operations within the control process.

The second part is constituted of separated modules used as inputs and outputs in the control process:

- 2 analog input modules NI 9215 with BNC connectors.
- An analog output module NI 9263 (not used).
- 2 digital input/output modules NI 9401 (only one in use).



Figure 4.10: CRIO 9022 controller with the used modules.

### 4.1.7. Control implementation

The control strategy used is explained theoretically in the Chapter 2 of the current thesis and implemented in the CompactRIO controller.

The programming of the CompactRIO controller is fully developed with Labview block diagram environment from National instruments. In order to perform an efficient control, the different tasks of the control strategy have been split between the FPGA block (takes place in the FPGA of the CompactRIO) and the processor block (takes place in the processor of the CompactRIO).

Fig. 4.11 shows the front panel where the variables of the system are monitored.

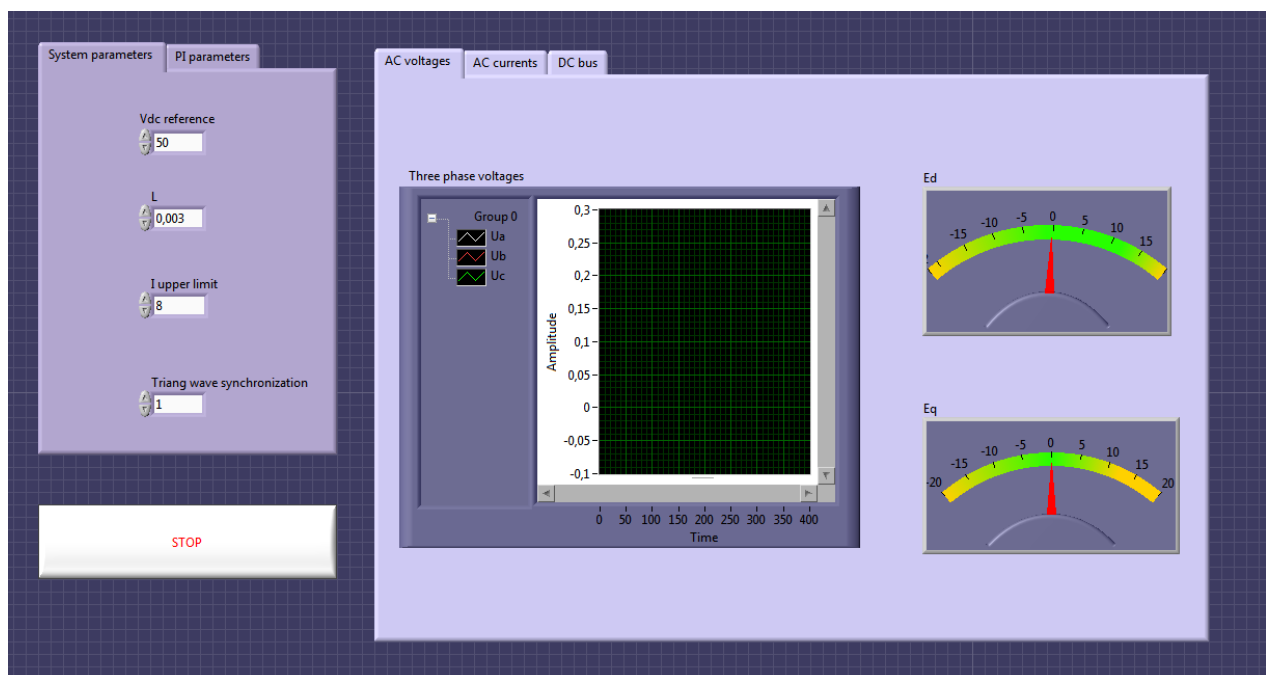


Figure 4.11: Labview front panel interface used for the control.

#### 4.1.7.1. FPGA block

In the FPGA, the tasks that require very high speed are implemented. These tasks are mainly a generation of 10 kHz triangular wave, the data acquisition (with the calculation of theta angle included) and the generation of the three PWM signals.

The generation of the three PWM signals for the control of each inverter leg is done through the comparison of the triangular wave and a reference voltage, in Fig. 4.12 below it can be observed how the comparison between the triangular wave and the reference voltage is done in a digital implementation case as the implementation in the FPGA.

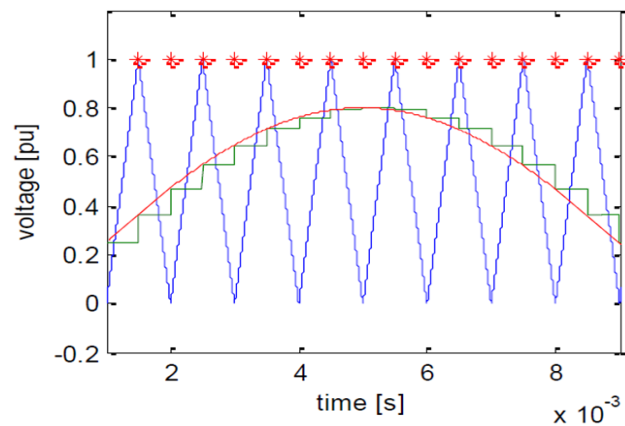


Figure 4.12: Schema of digital PWM generation in the FPGA.

In order to have proper measurement of the currents and voltages, triangular wave synchronization is used for being sure that all the operations in the system are synchronized with the 10 kHz triangular wave.

#### 4.1.7.2. Processor block

Due to the FPGA has limited resources, the whole control cannot be implemented in it. For this reason, some tasks are programmed in a processor block inside the CompactRIO processor.

In the processor the most complex operations are made, these operations consist in the dq transformations and the implementation of the decoupled control strategy explained in Chapter 2. Labview PI blocks are used in this stage for implementing voltages and currents controllers.

## 4.2. Results from the experimental setup

All the results are recorded with a scope LECROY Wavepro 715 and the results plotted in Matlab for generating the attached graphs.

### 4.2.1. Integrated charger based on a 2 kW Split-Phase PM motor

The experimental setup explained in the section above (Fig. 4.1) is tested for charging mode with an AC supply voltage of  $75 V_{LL}$ . The dynamic response against a step change is tested.

The controller is set to maintain a constant DC voltage in the DC bus of 100 V. Since the load is set in 50 Ohms and the DC current is constant 2 A, the integrated charger is charging the

battery with power transference of 200 W. In Fig. 4.13 the current and voltage in the battery side during charge operation are represented.

One of the purposes of the control stage is to charge the battery with unity power factor. In order to fulfill this purpose the value of  $i_q$  is set to zero.

In Fig. 4.14 it is shown that the currents have a sinusoidal waveform and since the  $q$  component of the current is zero, the  $d$  component of the current corresponds to the peak value of the sinusoidal wave. This value is approximately 4 A.

As can be observed in Fig. 4.15, the current through the machine remains in phase with grid voltage during the charging mode, keeping the unity power factor desired.

During the before explained charge operation, the voltage that is dropping in the machine winding is measured and plotted in Fig. 4.16. Since the system is controlled during charging time, the voltage drop in the machine remained sinusoidal (presenting some small ripple).

As can be observed in the Fig. 4.16, the voltage and the current remains almost in phase due to the motor parameters which in the configuration used (explained in Chapter 3) have a high resistive component.

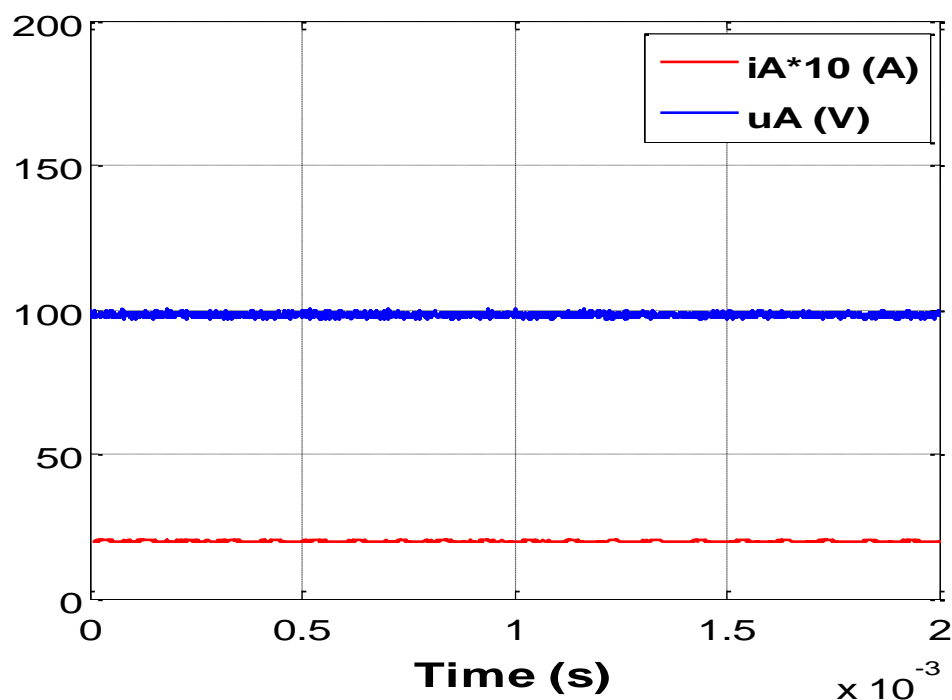


Figure 4.13: Current and voltage in the DC side for the tested charging time (2 kW motor).

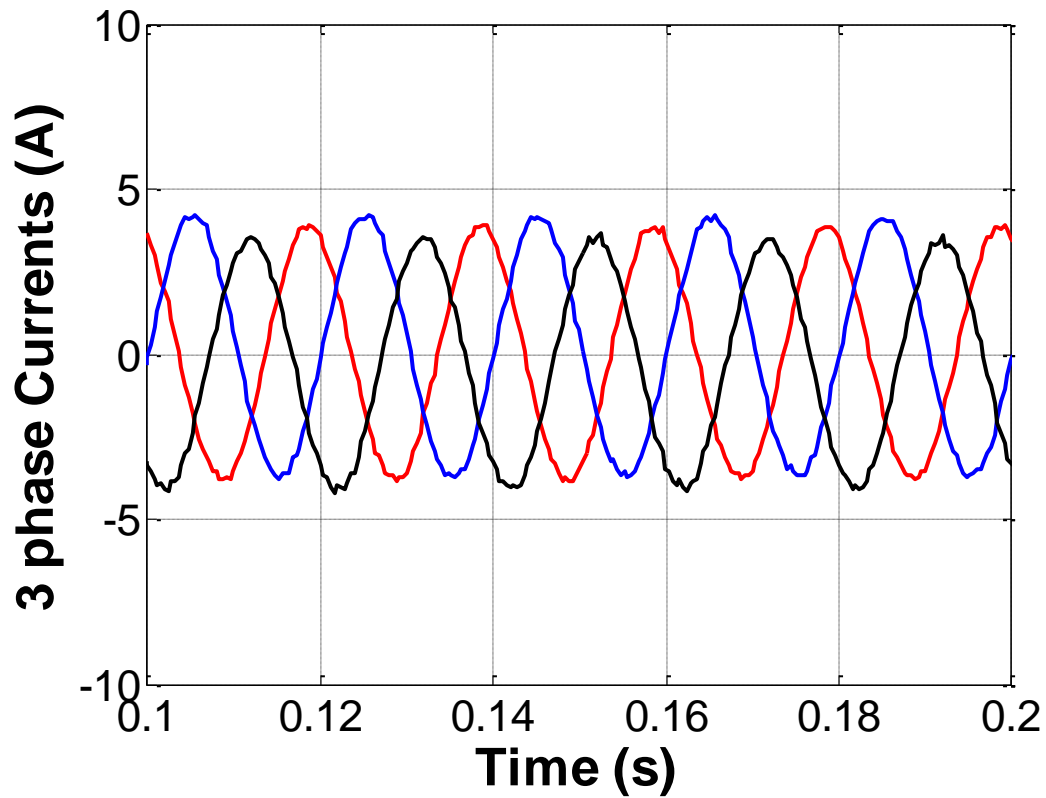


Figure 4.14: Three phase currents during charging time (2 kW motor).

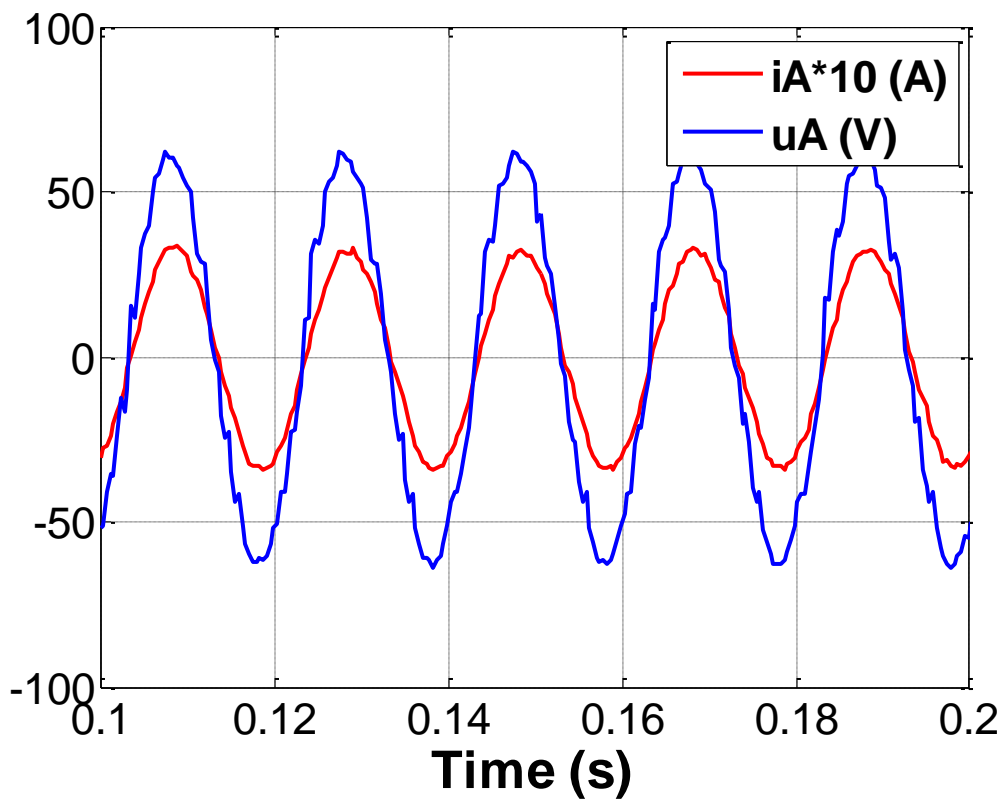


Figure 4.15: Current and voltage of phase A during charging time (2 kW motor).

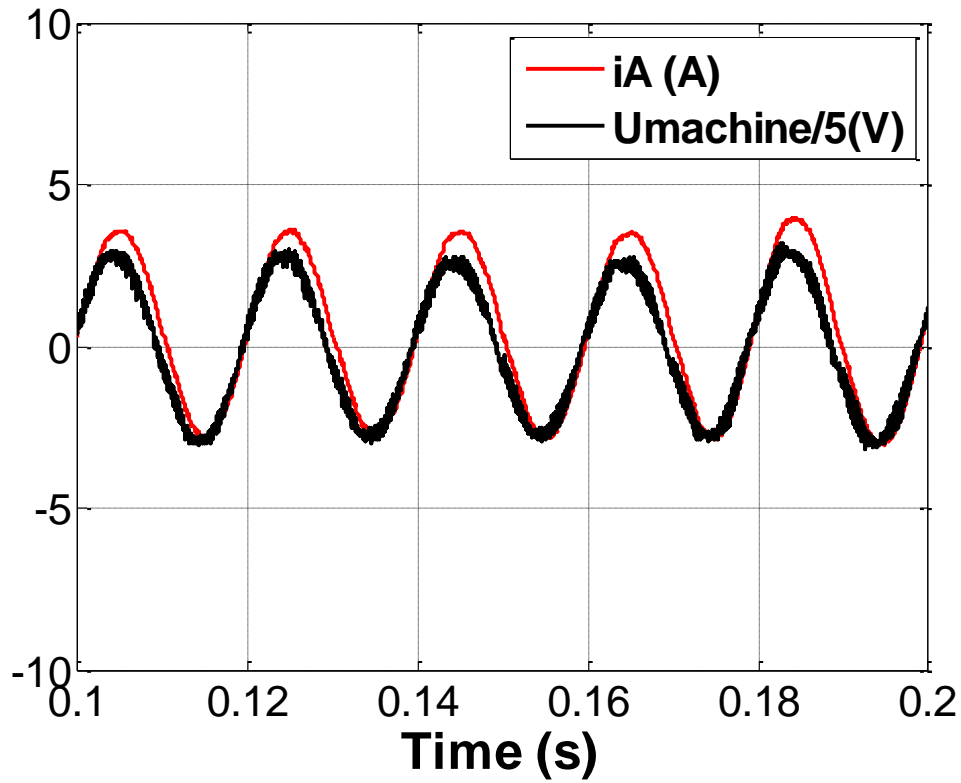


Figure 4.16: Current and voltage over the windings during the charging time (2 kW motor).

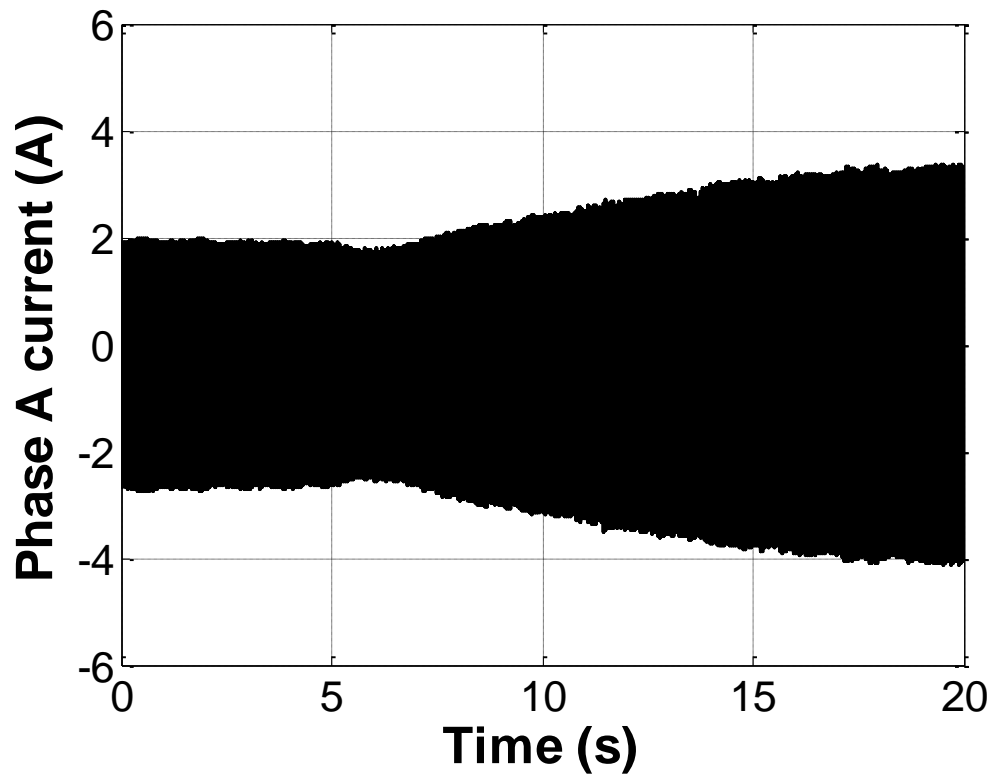


Figure 4.17: Response of phase A current against a step of the DC voltage reference (2 kW machine).

The behavior of the system against a change in the input reference has been also studied. A step is applied in the reference voltage of the DC side, changing the setting value from 65 V to 100 V. Fig. 4.17 shows this behavior where the step is applied at 6 s.

This change in the DC reference voltage means that the system has to change the power transferred to the battery from 112 W ( $75 V_{DC}$ ) to 200W ( $100 V_{DC}$ ).

The response of the system in terms of current in one of the phases is recorded and shown in Fig. 4.17.

#### 4.2.2. Integrated charger based on a 20 kW Split-Phase PM motor

The experimental integrated charger is also tested with the 20 kW PM motor explained in Chapter 3. The configuration for the windings is shown in the Fig. 4.2. During the whole test, the torque developed for the machine was around zero, so the machine remains in stand-still, without any movement in the rotor.

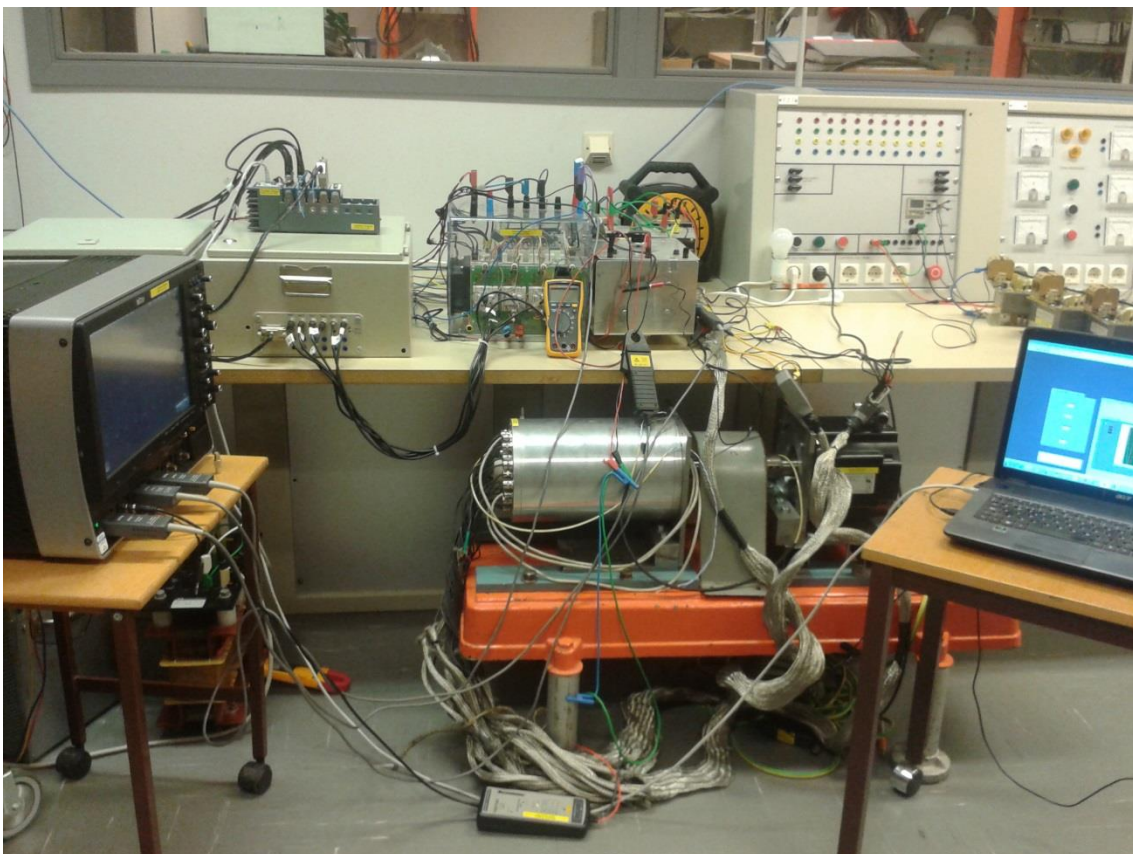


*Figure 4.18: Experimental setup using the 20 kW PM motor.*

A charge power of 200 W with a grid supply of 75  $V_{LL}$  is tested with a step change in the load.

The controller is set to maintain a constant DC voltage of 100 V. Since the load is set to 50 Ohms the DC current is observed as a constant current of 2 A. The results from the DC bus are shown in Fig. 4.19. In this case a small ripple in the DC side voltage is observed. The time scale in Fig. 4.19 has been reduced in order to show the ripple in the voltage more accurately.

The control stage in this setup has presented more difficulties than in the first one, mainly due to the inductance profile in the machine, which is a function of the rotor position. As a result of these difficulties the small ripple in the DC side voltage and an asymmetrical component in the currents are observed, as is shown in Fig. 4.20.

As in the previous case, one of the purposes of the control stage is to charge the battery with unity power factor and in order to fulfill this purpose the value of  $i_q$  is set to zero.

In Fig. 4.20, the currents remain with a controlled sinusoidal waveform and since the  $q$  component of the current was kept at zero value, the  $d$  component of the current corresponds to the peak value of the sinusoidal wave. This value corresponds to 3 A in this case.

Fig. 4.21 shows how the current remains in phase with voltage during the charging time, keeping the unity power factor desired.

As in the setup with the 2 kW motor, the measurements of the windings voltage drop are taken, the voltage drop in the windings represent a sinusoidal waveform with a peak voltage of 5 V. The waveforms of voltage and current over the windings are shown in Fig. 4.22 where can be seen a small phase shift between voltage and current over the windings, due to in this case the resistance value is lower than in the previous setup. Fig. 4.23 represents a zoom where the phase shift is shown. As can be observed in the figure, the current is slightly out of phase with the voltage. In the time scale this phase shift represents a value of 0.0001 s that means a phase shift of 18 degrees.

The behavior of the system against a change in the input reference has been also studied. In the  $t = 5$  s in Fig. 4.24, a step is applied in the reference voltage of the DC side, changing the setting value from 65 V to 100 V. This change in the DC reference voltage means that the system has to change the power transferred to the battery from 85 W ( $65 V_{DC}$ ) to 220W ( $105 V_{DC}$ ).

The response of the system in terms of current of one of the phases is recorded and shown in Fig. 4.24.

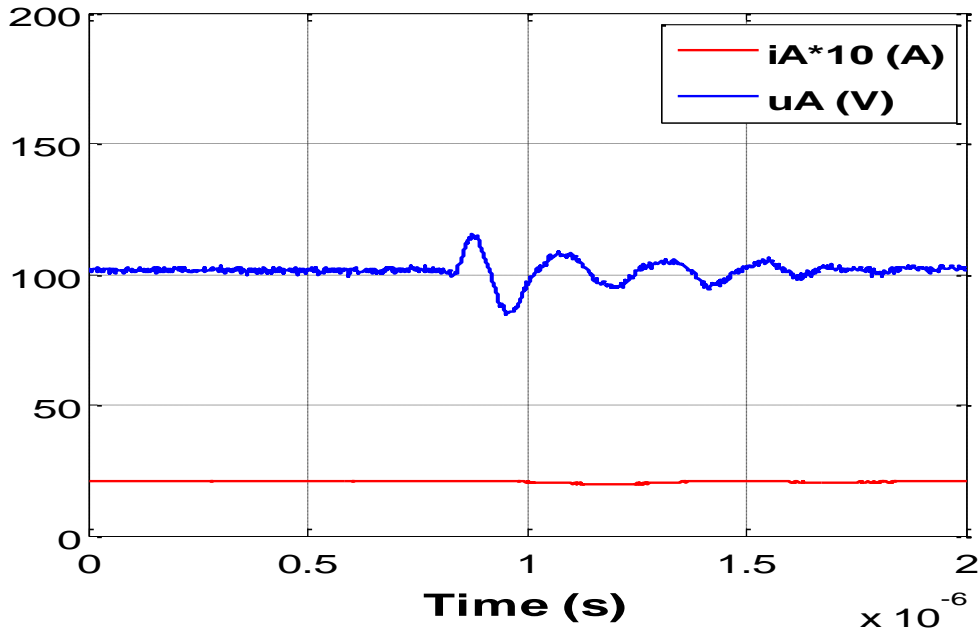


Figure 4.19: Current and voltage in the DC side for the tested charging time (20 kW motor).

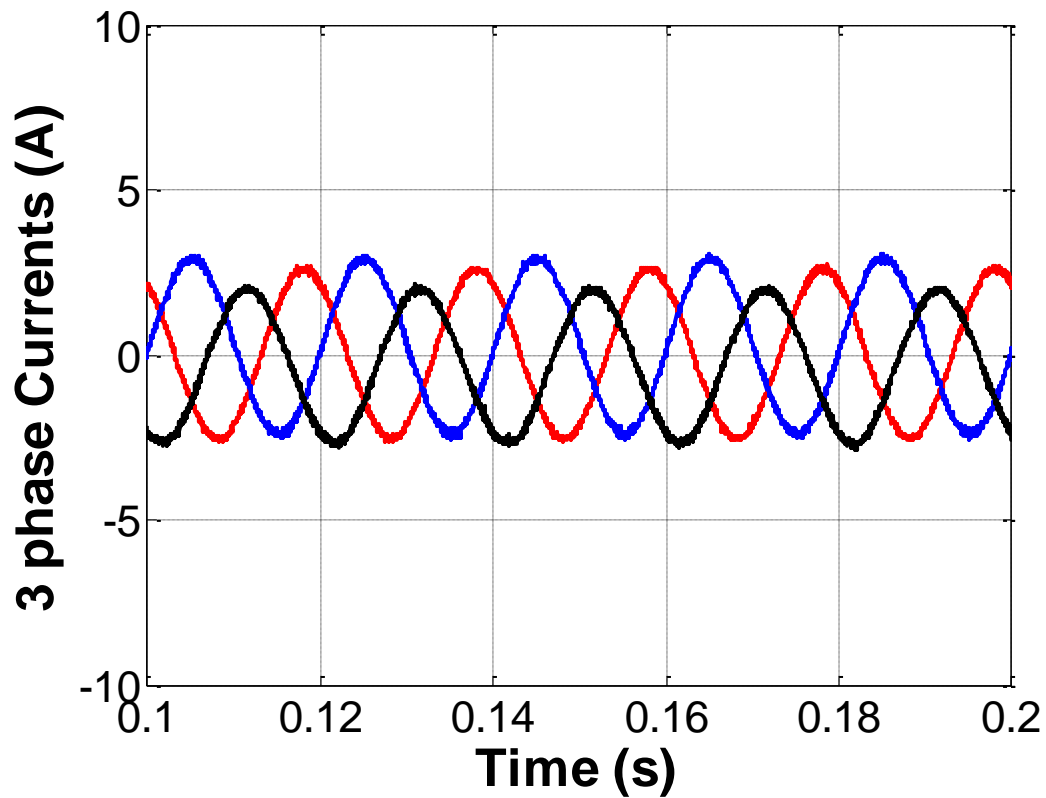


Figure 4.20: Three phase currents during charging time (20 kW motor).

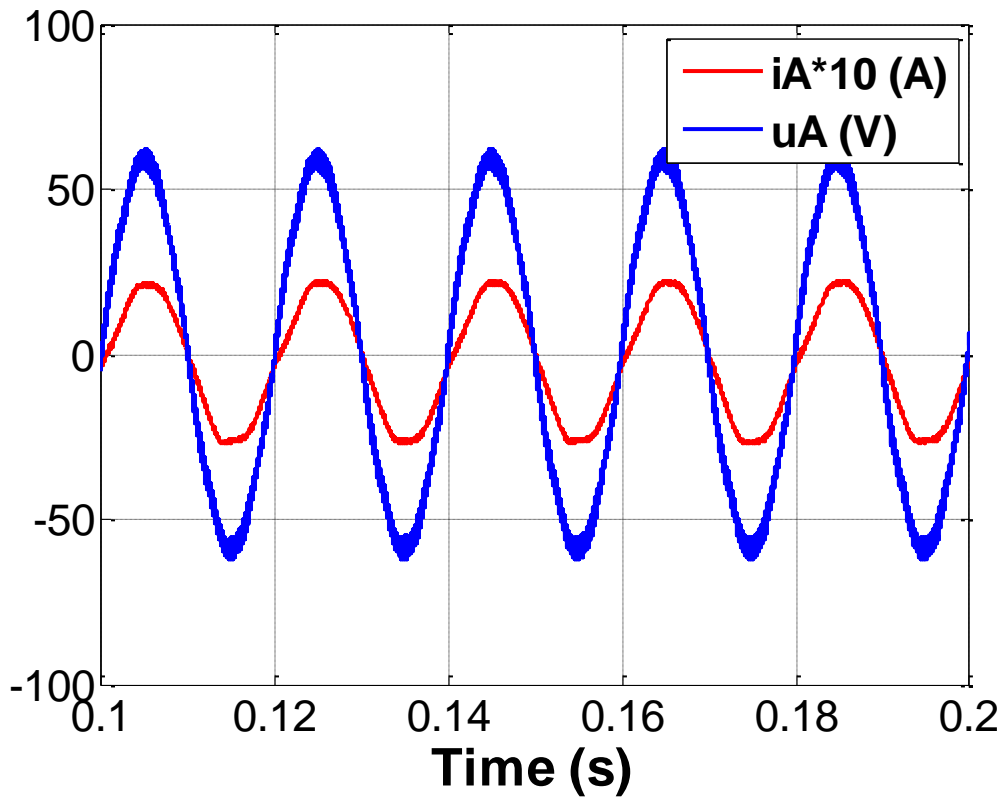


Figure 4.21: Current and voltage of phase A during charging time (20 kW motor).

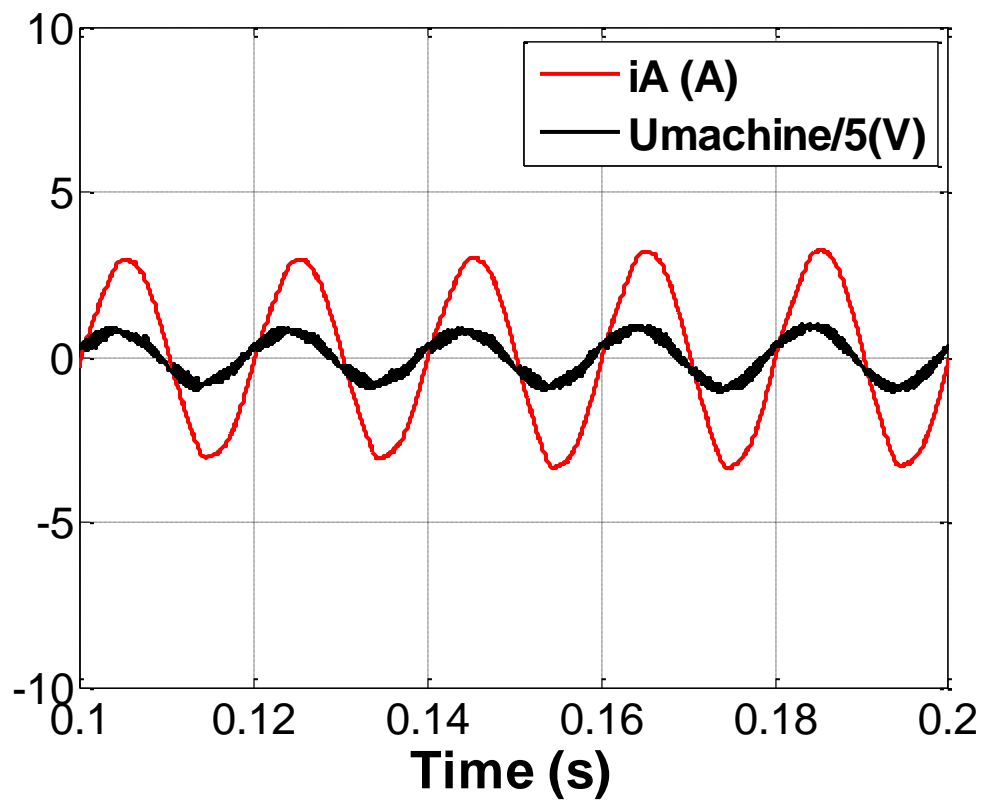


Figure 4.22: Current and voltage over the windings during the charging time (20 kW motor).

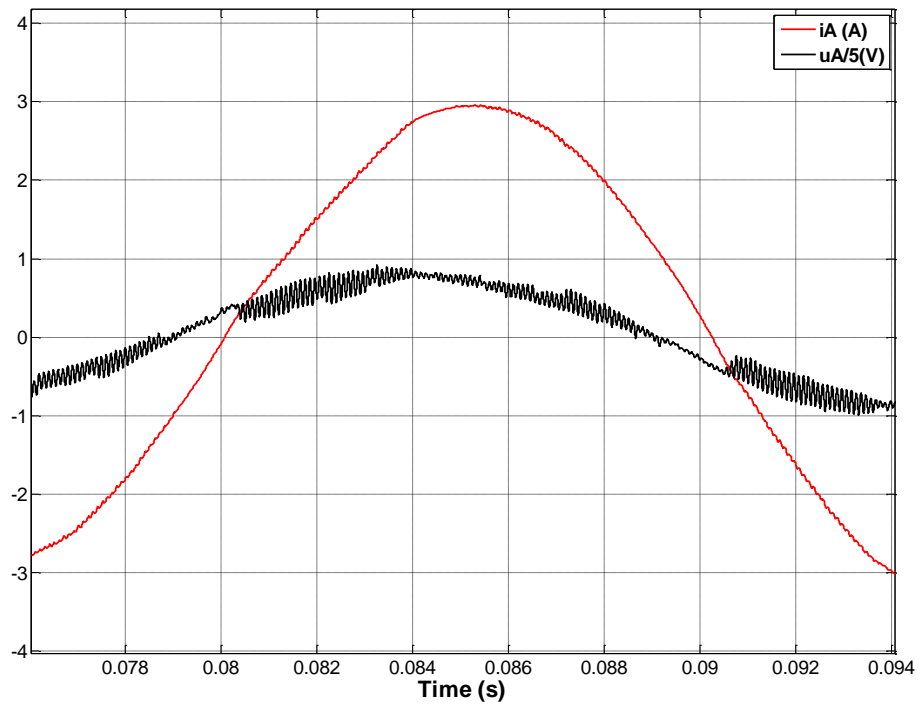


Figure 4.23: Phase-shift between current and voltage during charging time (20 KW motor).

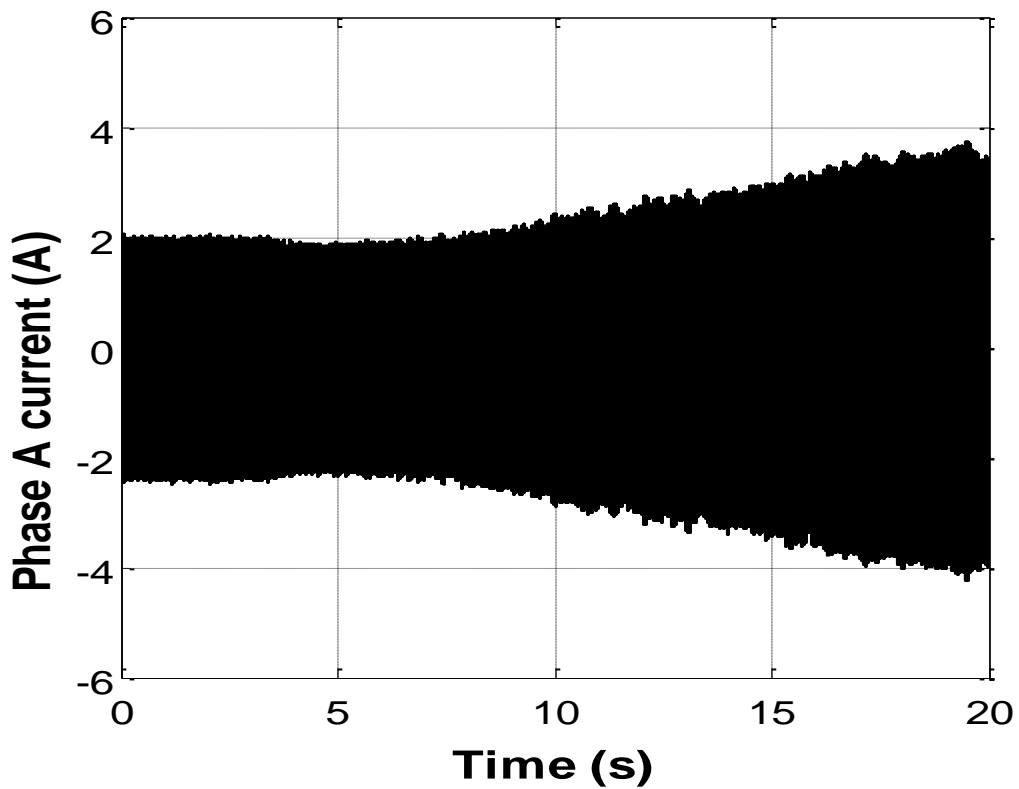


Figure 4.24: Response of phase A current against a step of the DC voltage reference (20 kW machine).

### 4.2.3. Discussions, limitations and improvements

The explained difficulties found in the control stage with the 20 kW PM motor due to the explained variable inductance profile and the problems with the noise at high voltages, make conclude that the 2 kW PM motor is more suitable for the implemented application since the control reached is more stable and the currents in the machine during the charging mode operation can be higher than the rated current, while in the 20 kW PM motor the currents are lower than the rated value due to noisy reasons.

Since the measurement transducers used have certain limits for the maximum AC supply and the maximum current, the power level in charging mode could not be increased much more than 200 W, so for future developments it is recommended to work with more powerful measurement devices.

Even though the charging mode operation had acceptable results, the dynamic behavior could be improved performing a control with faster response against a step change. During the testing of the control stage a lot of problems were found with the speed of the operations used in the CompactRIO controller (especially the ones carried out in the embedded processor), for future developments of the non-isolated battery charger, an implementation with another control hardware could be implemented like is reported in [1].



# Chapter 5. Conclusions and Future Work

---

## 5.1. Conclusions

A non-isolated integrated battery charger based on a split-phase PM motor with a possible application in electric vehicles or plug-in hybrid electric vehicles has been practically implemented and tested during the current thesis.

Firstly, some windings configurations for the machine during charging mode have been analyzed implemented and tested. In these configurations the mutual flux cancel out during charge operation, and therefore the developed torque for the machine during charging time is keeping in stand-still.

Furthermore, working with the developed simulations by previous studies as a support ([2] and [9]), the purposed integrated charger using two PM motors with the mentioned winding configuration were implemented in the lab. In order to perform the control of the battery charger, a CompactRIO control system is used. The control has been tested, enhanced and modified during the work trying to perform the most efficient control.

Finally, the results of the charge operation have been presented; the whole system had a satisfactory operation in steady state operation for a charge power of 200W. Requirements as unity power factor or currents under control could be reached. The behavior of the system against a change in the references has been analyzed as well. Also, the behavior of the machine during charging time has been shown and analyzed in Chapter 4.

## 5.2. Future work

The main challenge for improving the proposed model is the improvements in the control system. As is shown in the experimental setup part, the response against a change of the system was quite slow. Improving the control part, a faster and more stable response against a change in the load could be achieved. The extra inductance used in the experimental setup could be removed having a more realistic implementation.

Since the current control system based in the CompactRIO controller has not desirable performance, a possible option could be the implementation of the control strategy using another control device as dSpace for example, as is reported in [1].

The hardware used in the lab limits the current and voltage for the wires to a charge power around 200 W. For achieving a more realistic experimental setup, the battery power should be increased using measurement interfaces capable to handle higher power levels.



# References

---

- [1] S. Haghbin, “Integrated Motor Drives and Battery Chargers for Electric or Plug-in Hybrid Electric Vehicles,” PhD Thesis, Chalmers University of Technology, 2013.
- [2] S. Lechat Sanjuan, “Voltage Oriented Control of Three-Phase Boost PWM Converters”, Master of Science Thesis in Electric Power Engineering, Chalmers University of Technology, Göteborg, 2010.
- [3] Malinowski Mariusz. “Sensorless Control Strategies for Three-Phase PWM Rectifiers”. PhDThesis, Warsaw University of Technology, Faculty of Electrical Engineering, Institute of Control and Industrial Electronics. Warsaw, Poland. 2001. 128p.
- [4] S. Haghbin, I. Serrano Guillén, “Integrated motor drive and non-isolated battery charger based on the torque cancellation in the motor,” *IEEE International Conference on Power Electronics and Drive Systems*, 2013.
- [5] S. Haghbin, T. Thiringer, O. Carlson, “An integrated split-phase dual-inverter permanent magnet motor drive and battery charger for grid-connected electric or hybrid vehicles,” *Electrical Machines (ICEM), XX International Conference on*, Sept. 2012.
- [6] S. Haghbin, S. Lundmark, M. Alakula, and O. Carlson, “An Isolated High-Power Integrated charger in electrified-vehicle applications”, *Vehicular technology, IEEE Transactions on*, vol. 60, no. 9, pp. 4115-4126, nov. 2011.
- [7] S. Haghbin, K. Khan, S. Zhao, M. Alakula, S. Lundmark, and O. Carlson “An integrated 20 kW motor drive and isolated battery charger for plug-in vehicles,” *Power Electronics, IEEE Transactions on*, vol. 28, no. 8, pp. 4013-4029, aug. 2013.
- [8] K. Khan, “Design of a permanent-magnet assisted synchronous reluctance machine for a plug-in hybrid electric vehicle,” Licentiate Thesis in School of Electrical Engineering, KTH, Stockholm, 2011.
- [9] J. Mandiola, D. Carmona, “Design and Implementation of a Three-Phase Boost Battery Charger with PFC using CompactRIO Control System,” Master of Science Thesis Power in Electric Power Engineering, Chalmers University of Technology, Göteborg, 2012.
- [10] Getting started with CompactRIO and Labview, National Instrument Webpage.
- [11] Vindel Muñoz D., “Design, Simulation and implementation of a PMSM drive system,” Master of Science Thesis in Electric Power Engineering, Chalmers University of Technology, Göteborg, 2011.

- [12] S. Haghbin, R. Ghorbani, A. Bermejo Fernández, I. Serrano Guillén, “An Integrated Motor Drive and Battery Fast Charger Station for Plug-in Vehicles,” *IEEE International Conference on Power Electronics and Drive Systems*, 2013.
- [13] SEMITEACH – IGBT SKM 50 GB 123D, Datasheet.
- [14] CompactRIO analog input module. NI 9215 module for using with NI CompactDAQ and CompactRIO.

# Appendix A: User Guide for the Developed Software of the Non-isolated Battery Charger

---

In this appendix it will be explained how to run the software from the beginning. Practical instructions for running and operating the system are explained.

## A.1. Software installation in the computer

Before running the system, the National instrument software that the controller uses should be installed in the computer. The software needed for a proper operation with the CompactRIO in the battery charger project is:

### *1. LabVIEW modules and toolkits:*

- LabVIEW 2012 (+f3 patch)
- Real time module (+f1 patch)
- FPGA module (+f1 patch)
- NILV 2012 Electric power functions

### *2. NI devices drivers*

- NI 96If1
- NIRIO120 (NiRIO Dev.drivers August 2012)

**NOTE:** *If the user is working at Chalmers, two CDs with the mentioned software are available in the lab.*

Once all the software have been installed in the computer, the CompactRIO controller should be installed. For installing the CompactRIO controller, the user should connect the system to the computer through an Ethernet cable.

When the CompactRIO is connected to the computer, the user should launch MAX (Measurement & Automation Explorer) that is installed in the computer with the software explained before.

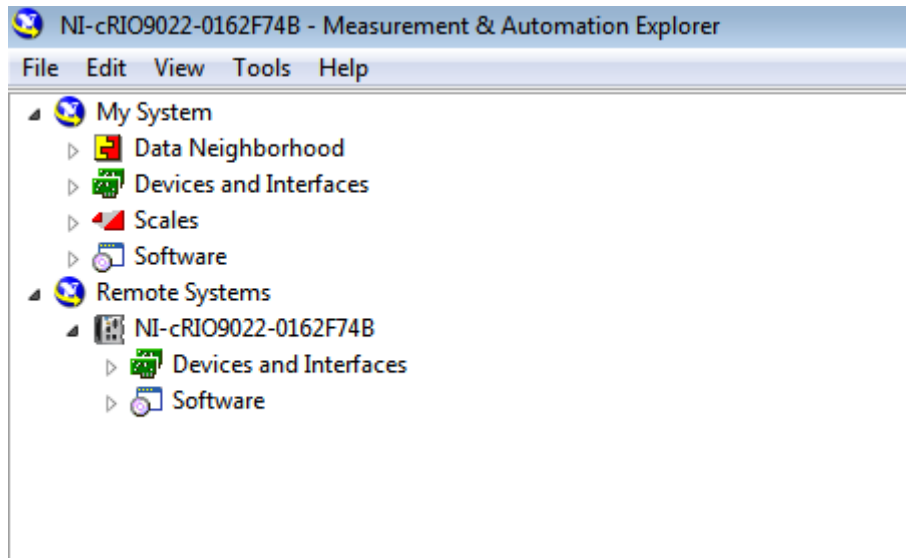


Figure A.1: Main screen of MAX.

In the main screen of MAX (Fig. A.1), under Remote systems, the CompactRIO controller should appear connected. If it does not appear, some typical solutions for typical problems with the connection of the device can be found in [10].

## A.2. CompactRIO installation

When a new CompactRIO is installed for the first time, it is recommended to format the old files inside the controller and install the new ones that are installed inside the computer. In order to install the software, the user should manually set the controller in safe mode (as is shown in Fig. A.2).

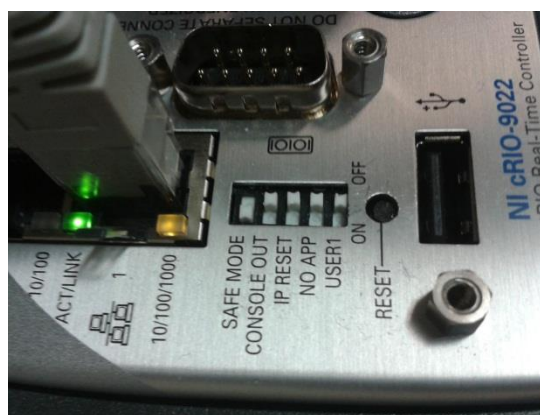


Figure A.2: CompactRIO set in safe mode.

Inside MAX and with the controller in safe mode, right click in the icon of the controller (in Fig. A.1 NI-cRIO9022-0162F74B) and select 'Format disk' in order to install it. After this

MAX will start to format the controller. Once MAX has finished formatting the disk, the new software is ready to install. Before installing the new software, the controller should be returned out of safe mode.

With safe mode OFF, expand the controller item tree and right-click on ‘Software’ selecting ‘Add/Remove software’. For working in the battery charger project, all the files that appear in Fig. A.3 should be installed.

When the installation is finished, the controller will perform a reset and after it will perform the connection another time automatically. Fig. A.3 shows the view of the controller in MAX after a successful software installation.

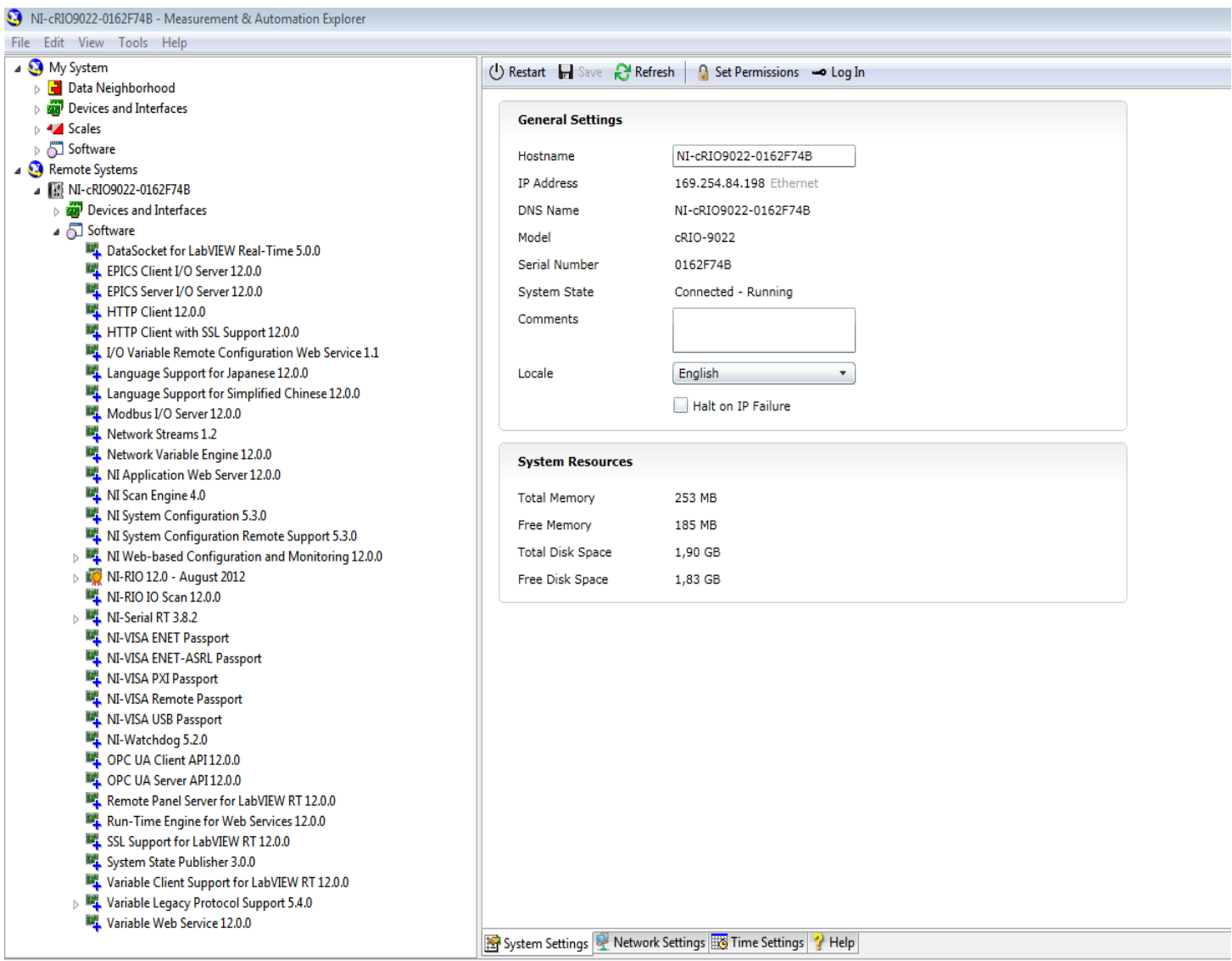


Figure A.3: Main screen of MAX when the CompactRIO software is fully installed.

Once all the above steps are done, the controller will be prepared for being added into a LabVIEW project and the main screen of MAX should be as in Fig. A.3.

**NOTE:** During the current thesis, all the work with the CompactRIO has been carried out using a private laptop. Since, a ‘Local IP connection’ (connection for a private laptop) was used, any issue related with IP address is explain in this guide, is highly recommended for beginner users connecting the controller through a private laptop as was done during this thesis, just to try to avoid conflicts with the IP address. With this kind of connection the controller is directly connected with the Ethernet cable to the computer, however, it will not be possible, to access the controller from another computer different that the mentioned laptop.

### A.3. Adding the new compactRIO controller to the LabVIEW project

Once the controller is recognized by the computer and all the required software is installed inside the controller, it is time to add the controller to the LabVIEW project.

For the current project, all the LabVIEW files can be found in a folder called ‘Integrated ChargerCompactRIO’, in order to run the system. A LabVIEW project file symbolizes a kind of summarize of the whole project, where the user can have access to the project VIs.

When the project file is opened, the user will observe that a CompactRIO device is already inside the project, but for working with the current compactRIO that has been installed, it has to be added to the project. The user should right click on the top icon for the project explorer, as is shown in Fig. A.4.

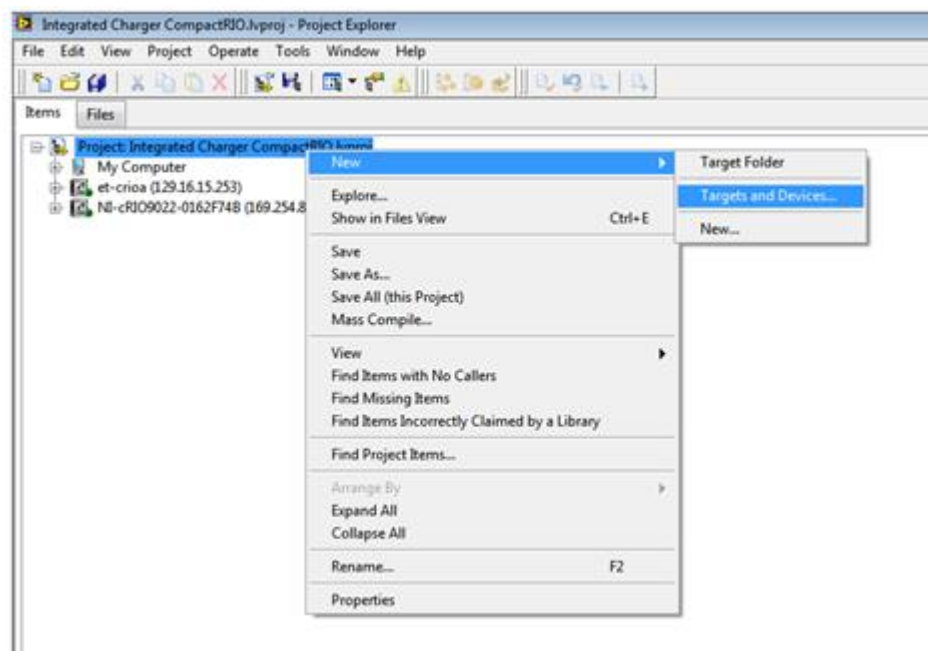


Figure A.4: How to add the new CompactRIO in the project.

Keeping the option ‘Discover an existing target(s) or device(s)’, the connected CompactRIO will appear under the option ‘Real-Time CompactRIO’, as seen in Fig. A.5.

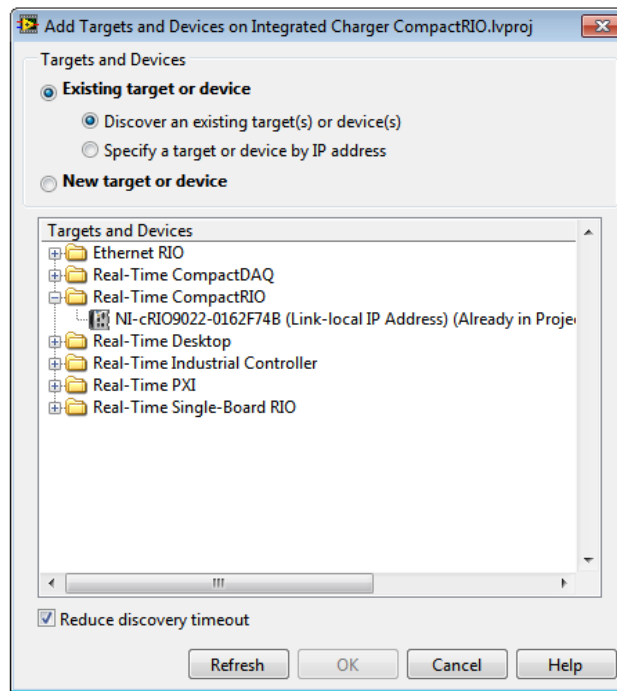


Figure A.5: Discovering the CompactRIO device in LabVIEW.

Since the project for the current thesis uses the FPGA, the user should select the option ‘Create New CompactRIO FPGA Project’.

After performing all the operations above, the new CompactRIO controller will appear below the one that was already in the project.

#### A.4. Deploying the VIs

Once the new controller is added to the current project, the different VIs used should be moved to the new controller. First the FPGA VI called ‘IntegratedChargerFPGA’ and the two FIFOs placed under the FPGA of the first CompactRIO should be drag and dropped to the FPGA of the new CompactRIO. After, the rest of the VIs should be drag and drop under the CompactRIO chassis. As a result of this process, the project should look like as Fig. A.6.

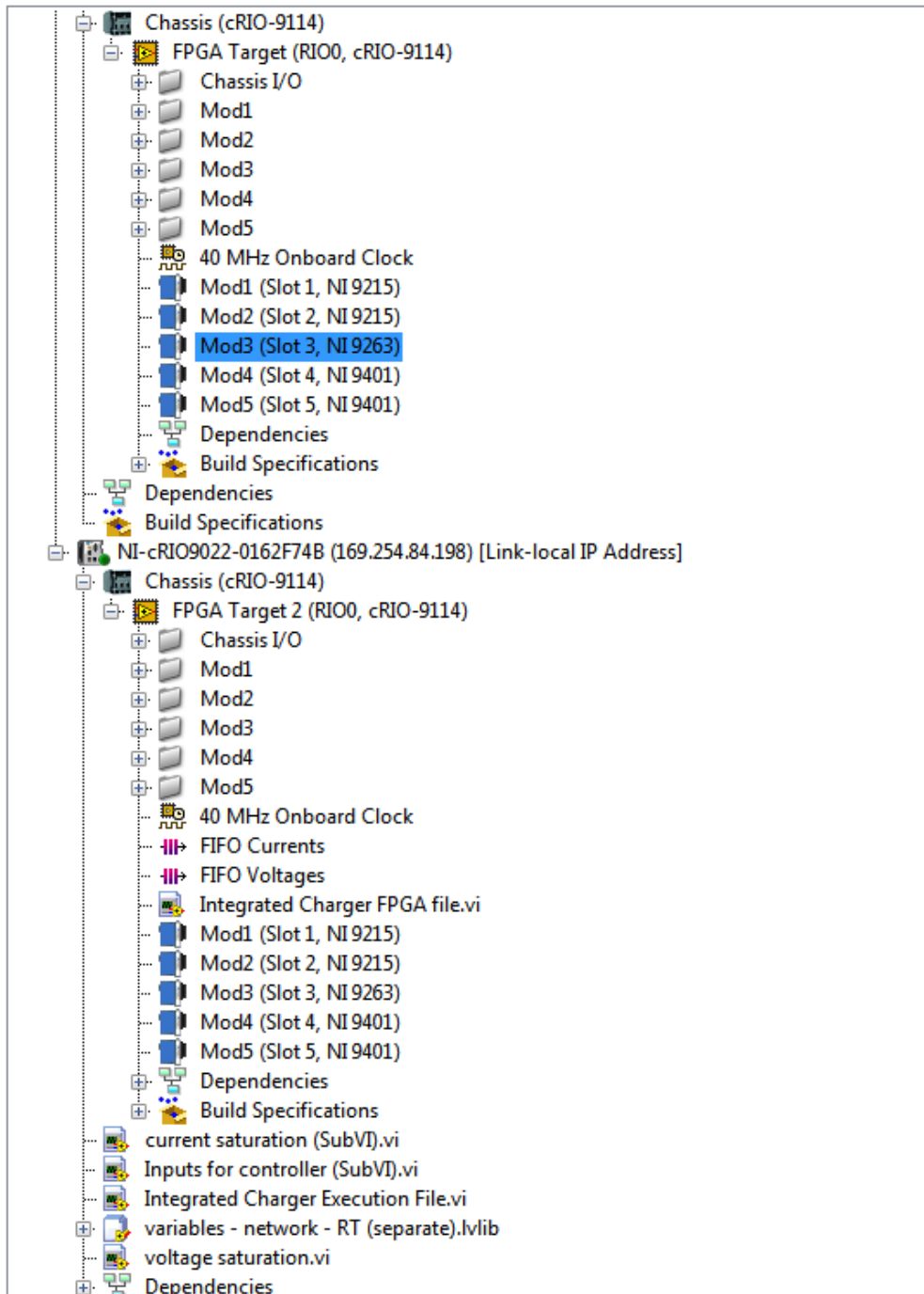


Figure A.6: View of the project explorer after move the files.

As can be observed in Fig. A.6, the first CompactRIO that was in the project is empty, and all the VIs appear under the new one. After this step, the first CompactRIO could be removed from the project if it is desired.

## A.5. Renaming the modules

In the Labview program, the different inputs and outputs of the system have the name of the variable that it is connected to, so the AI0 of the module 1 is called Ua and not AI0 by example. For satisfying this requirement in the new installed CompactRIO, the different inputs and outputs for the modules should be renamed as the names were named in the first CompactRIO (the user just need to write the same name that it is in the original CompactRIO module). The names should be as in Fig. A.7. For a block in a module, right click on the block and select 'Rename'.

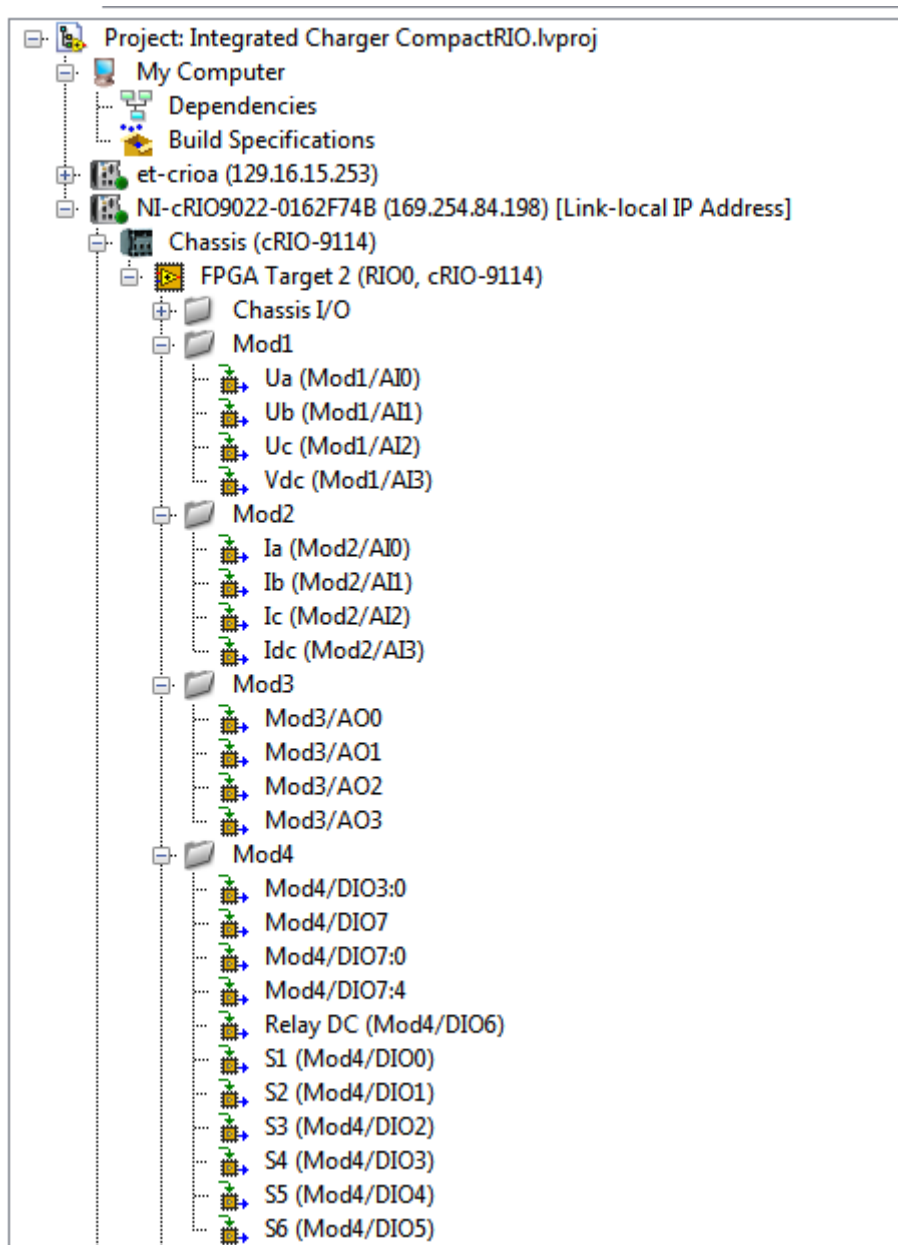


Figure A.7: Names for the inputs and outputs in CompactRIO modules.

The CompactRIO digital modules can be used as digital input or as digital output, but are configured as an input by default. In the integrated charger project the digital module is used as an output, so the line direction of the module should be changed. In order to do this, right click on the icon of module 4 and change the line direction to output, see (Fig. A.8).

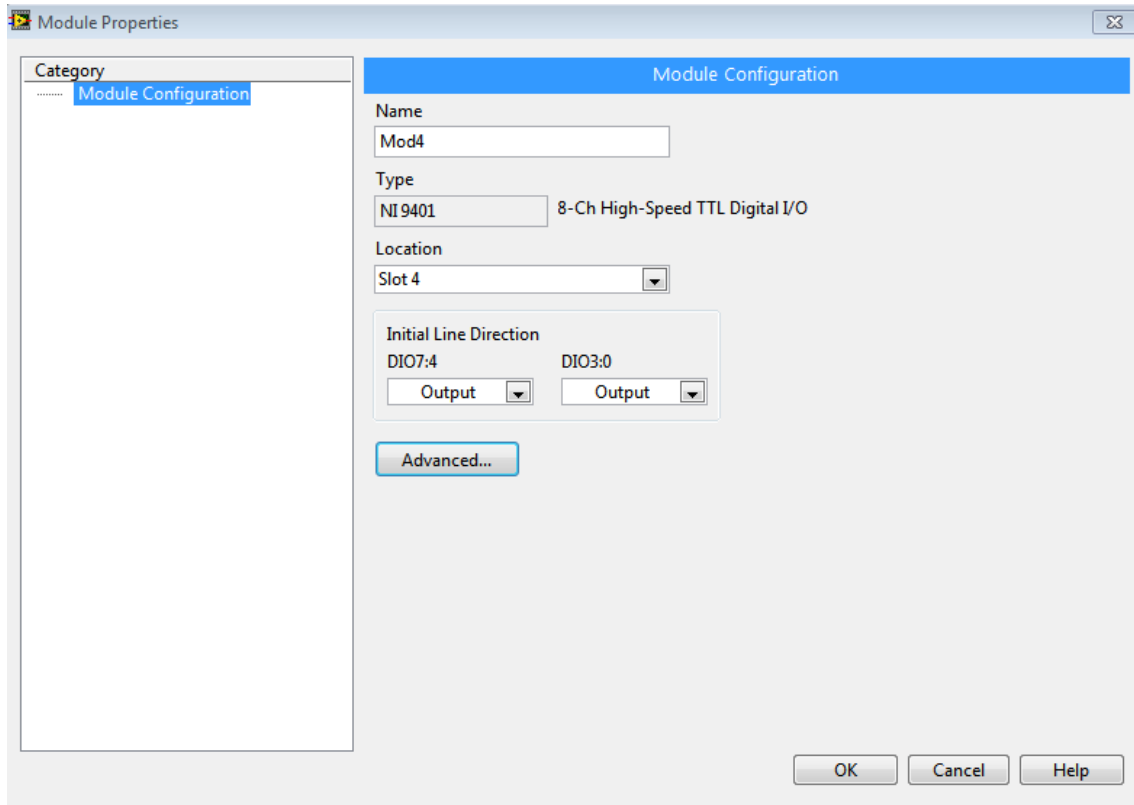


Figure A.8: How to change the initial direction for the digital module used.

## A.6. Compiling the FPGA file

Before running the system, the FPGA VI should be compiled. The user just need to open the FPGA VI and run it, the window for compiling the file will appear. Since a compiler in the computer has been installed (Xiling 13.4), the option 'Compile with a local compile server' should be selected and the FPGA file will start to compile (the compiling process take some time, normally around 45 minutes).

**NOTE:** *If the modules are not named correctly, the program will not be able to compile the FPGA, if this is the case, the names of the different modules should be reviewed.*

## A.7. Running the system

After performing the steps above, the system is ready to run. Every part of the system should be powered, a detailed explanation about how to connect the system can be found in the Chapter 4 of the current thesis.

When all the devices are connected and the system is powered, the file ‘Integrated charger execution file’ can be run. Observing the three phase voltage in the front panel, it should look as Fig. A.9.

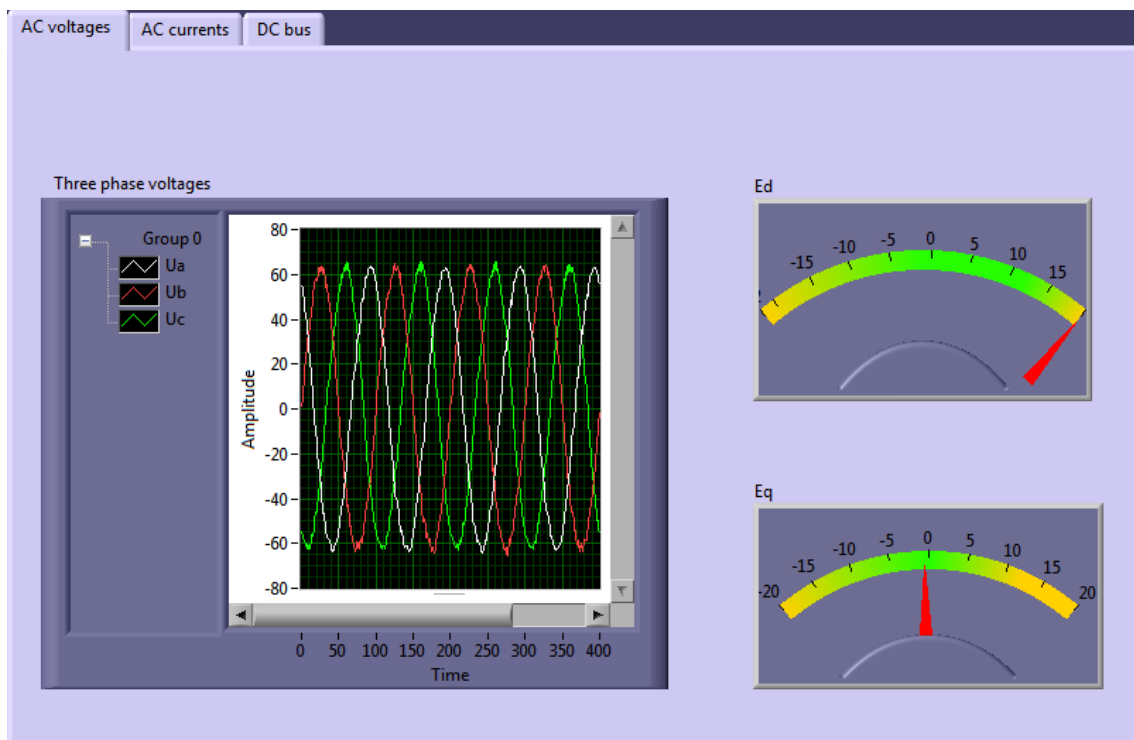


Figure A.9: View of the front panel when the system is running properly.

It is important to connect the phases of the system in the right order, this means that the phase A in the inverter should match with the phase A in the transformer. Since the three phases have different colors (blue, black and brown), they are easy to distinguish. For example, if the blue phase is connected in the phase A of the inverter, the blue phase should be connected in the phase A of the transformer as well. A probe of this setup is a right dq transformation (if the phases are correctly connected, the value of the Ed transformation will remain constant and the value for the Eq transformation will remain in zero, as can be seen in Fig. A.9).

## A.8. Changing system parameters

Some parameters can be changed before or during the program execution, parameters as inductance of the system, values for the PI controllers or limit of the current.

- *Inductance of the system*

The inductance of the system should be specified in Henry in the front panel to be used in the control stage. Theoretical explanation about the control stage of the system can be found in Chapter 2 of the current thesis.

- *PI parameters*

The PI parameters can be adjusted from the front panel, the values  $K_{pv}$  and  $T_{iv}$  correspond to the proportional gain and the integral time (**not integral gain**) for the voltage controller respectively. The values  $K_{pi}$  and  $T_{ii}$  correspond to the proportional gain and the integral time (**not integral gain**) for the current controller respectively. The explanation about how to calculate these values as a function of the physical values of the system can be found in [2].

- *Limit of the current*

This parameter, in Amperes, can be changed in the front panel as the other parameters and will indicate the maximum current accepted in the system.

# Appendix B. Experimental Setup for the Motor Parameters Measurement

This appendix explains the experimental setups performed for measuring the parameters in both machines, the 2 kW and the 20 kW PM motors. Different winding configurations were tested and analyzed.

## B.1. 2 kW PM motor

The 6 poles PM motor described in more details in Chapter 3 is studied in order to know the value of the inductance and resistance. The setup performed is shown in Fig. B.1.

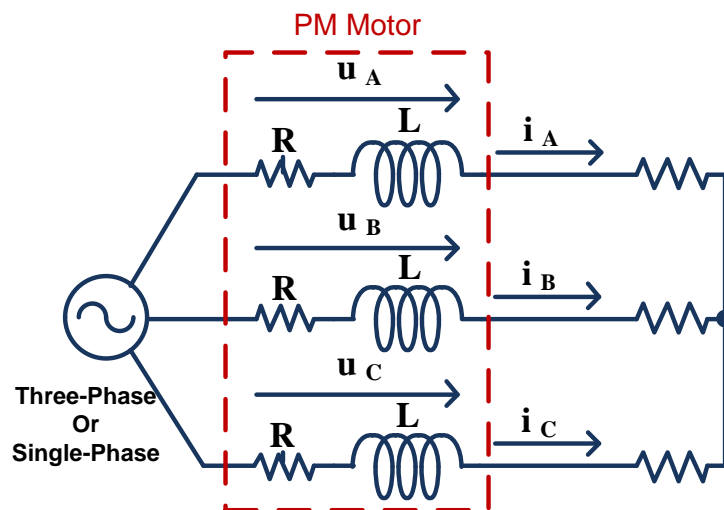


Figure B.1: Experimental setup for the inductance measurement.

As explained Chapter 3, the zero torque condition is a very important requirement for the integrated battery charger and to achieve it, the midpoints in the motor windings are used.

All the connections tested fulfill the zero torque condition but regarding the experimental setup performed in Chapter 4, not all of them are valid. The reasons and the election of the configuration can be found in Chapter 3.

The elements used in the setup described on Fig. B.1 are: a three-phase autotransformer, the 2 kW PM motor and a three-phase potentiometer. The measuring devices are two multimeters, one for measuring the voltage in the inductance of the machine and the other for measuring the current through it.

### B.1.1. Serial Connection

The detailed connection of the motor windings is described in Fig. B.2.

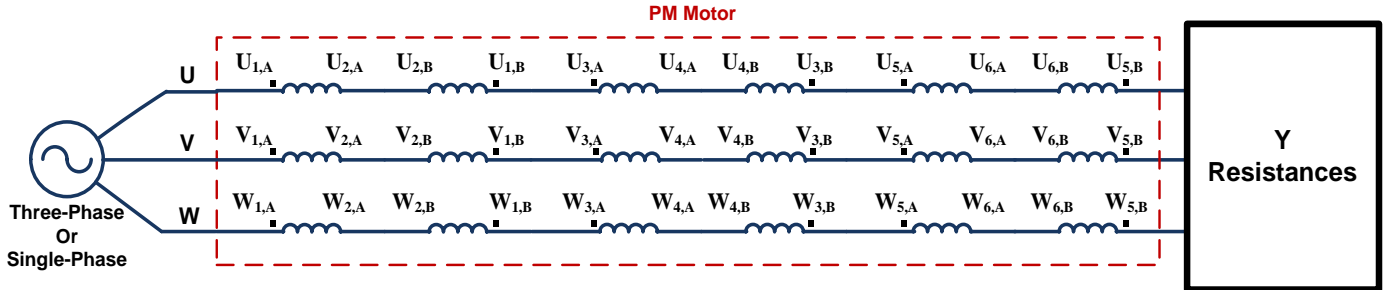


Figure B.2: Serial winding connection for 2 kW PM motor.

The measurement of the resistance is done through a simple circuit, feeding the machine with a DC source and measuring the DC voltage and current. The results obtained are:

$$\left. \begin{array}{l} \text{Phase A} \quad R = \frac{V}{I} = \frac{21.51V}{1.5A} = 14.34 \Omega \\ \text{Phase B} \quad R = \frac{V}{I} = \frac{21.45V}{1.5A} = 14.3 \Omega \\ \text{Phase C} \quad R = \frac{V}{I} = \frac{21.47V}{1.5A} = 14.31 \Omega \end{array} \right\} R = 14,31 \Omega.$$

The calculations for obtaining the inductance of the machine are detailed as follow:

$$|V|^2 = (R^2 + L^2 \omega^2) |I|^2 \quad (B.1)$$

$$\omega = 2\pi 50 \text{ rad/s.}$$

The inductance result for the serial connection is:

$$\left. \begin{array}{l} \text{Phase A} \quad \left. \begin{array}{l} V = 23.02V \\ I = 1.5A \end{array} \right\} L = 17.73 \text{ mH} \\ \text{Phase B} \quad \left. \begin{array}{l} V = 16.5V \\ I = 1.07A \end{array} \right\} L = 18.37 \text{ mH} \\ \text{Phase C} \quad \left. \begin{array}{l} V = 23.17V \\ I = 1.46A \end{array} \right\} L = 21.9 \text{ mH} \end{array} \right\} L = 19.33 \text{ mH.}$$

During the test, the behavior against different position of the rotor was studied, and it was observed that rotating the rotor do not suppose big changes in the results, i.e. the value of the inductance is constant.

### B.1.2. Parallel Connection: first configuration

For a parallel winding connection, there are two possibilities. The first one is shown in Fig. B.3.

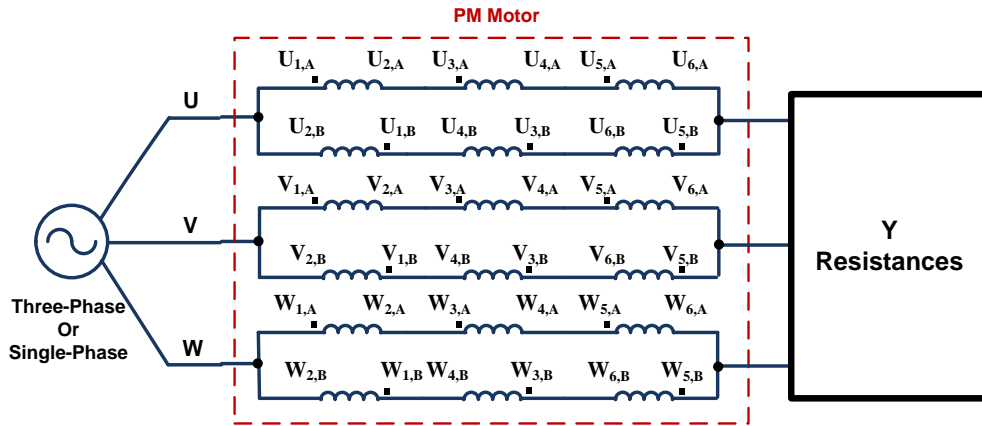


Figure B.3: First parallel winding connection for 2 kW PM motor.

The measurement of the resistance and the inductance are the same as it is described above for the serial connection. The results obtains for this first configuration are:

$$R = 3.5775 \Omega$$

Phase A	}	$V = 5.7 V$	}	$L = 4.12 mH$	$L = 4.64 mH.$
	}	$I = 1.49 A$			
Phase B	}	$V = 3.63 V$	}	$L = 4.45 mH$	
	}	$I = 0.94 A$			
Phase C	}	$V = 5.8 V$	}	$L = 5.34 mH$	
	}	$I = 1.46 A$			

The experimental measurements were recorded by the LECROY Wavepro 715 Oscilloscope and plotted using Matlab. Fig. B.4 shows the three phase voltages and the current in phase A.

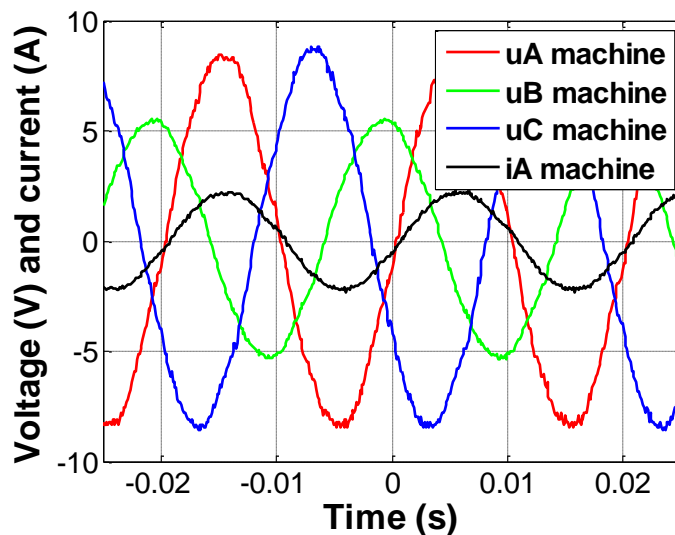


Figure B.4: Voltages and current in the measurement setup of the first parallel winding connection.

### B.1.3. Parallel Connection: second configuration

The second configuration for parallel winding connection is shown in Fig. B.5.

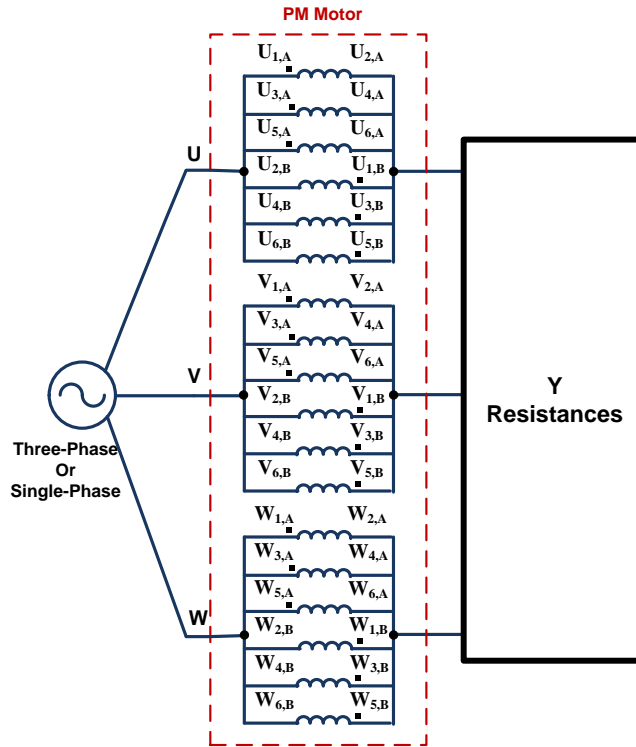


Figure B.5: Second parallel winding connection for 2 kW PM motor.

Measuring and calculating as for the previous configurations, the results for the second parallel winding connection are:

$$R = 0.3975 \Omega$$

$$\left. \begin{array}{l} \text{Phase A} \\ \text{Phase B} \\ \text{Phase C} \end{array} \right\} \begin{array}{l} \left. \begin{array}{l} V = 0.805 \text{ V} \\ I = 1.52 \text{ A} \end{array} \right\} L = 1,114 \text{ mH} \\ \left. \begin{array}{l} V = 0.532 \text{ V} \\ I = 0.91 \text{ A} \end{array} \right\} L = 1,3645 \text{ mH} \\ \left. \begin{array}{l} V = 0.946 \text{ V} \\ I = 1.48 \text{ A} \end{array} \right\} L = 1,593 \text{ mH} \end{array} \right\} L = 1.357 \text{ mH.}$$

As for the first configuration of parallel connections the results of the measurements are plotted in Fig. B.6.

Compared to the previous graph the three phase voltages are much lower, but the current through the machine is the approximately same.

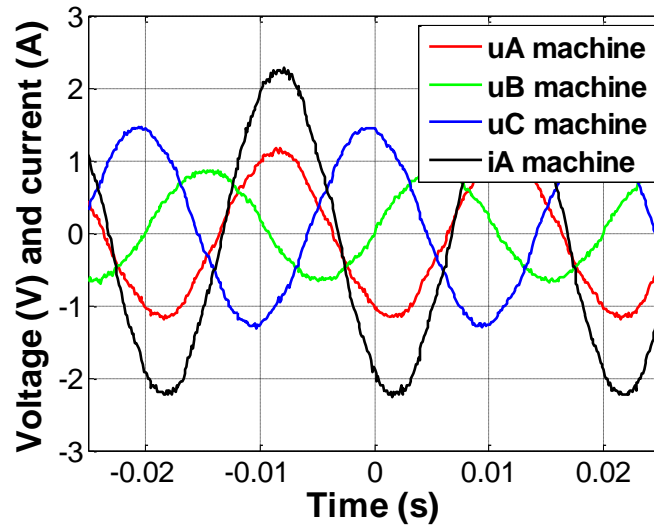


Figure B.6: Voltages and current in the measurement setup of the second parallel winding connection.

## B.2. 20 kW PM motor

For the 4 pole 20 kW PM motor described in Chapter 3, the experimental setup performed to measure the inductance is different. In this case a practical setup is used for testing a non-isolated integrated charger based in a diode rectifier [4].

As is explained in Chapter 2, this setup fulfills with the zero torque condition during the charge operation and for that reason it is possible to use the split phase PM motor as inductors, like in the experimental setup tested in the current thesis and explained in Chapter 4.

A main diagram of the setup is shown in Fig. B.7. The reason for testing the non-isolated integrated charger with that configuration is for simplicity and easy control. The elements of the setup are: a three phase autotransformer, a bridge rectifier, the 20 kW PM motor, a large capacitor and a three phase potentiometer.

As for the 2 kW PM motor, different winding configuration are tested, and the calculation of the inductance is performed.

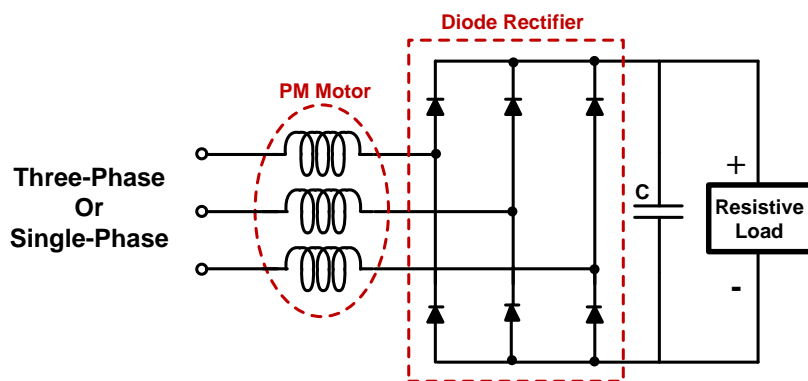


Figure B.7: Diagram of the practical setup for testing a non-isolated integrated charger.



Figure B.8: Practical setup performed for 20 kW PM motor.

### B.2.1. Serial Connection

The connection of the PM motor for a serial configuration is shown in Fig. B.9.

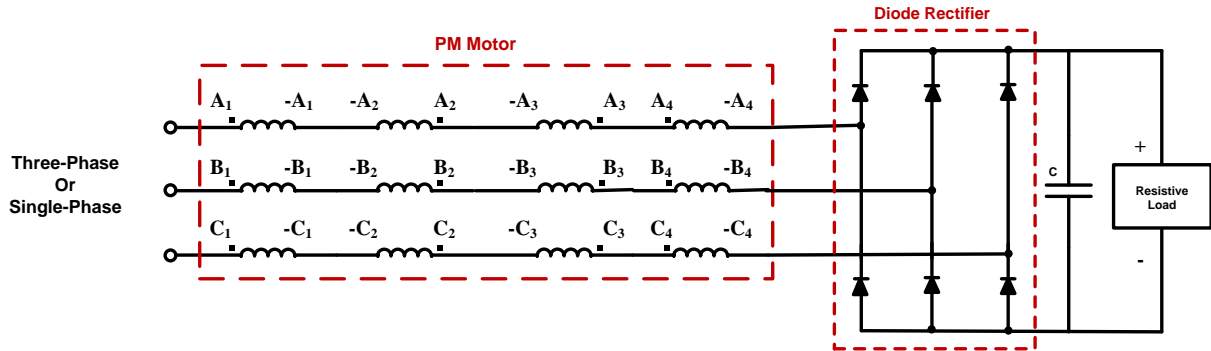


Figure B.9: Serial winding connection for 20 kW PM motor.

The value of the total resistance is known for previous studies [11], and in this configuration it corresponds to:

$$R = 1.6 \Omega.$$

The value of the inductance is calculated by equation (B.1), as in the case of 2 kW PM motor, and the result is:

$$\left. \begin{array}{l} V = 282.88 \text{ V} \\ I = 4.95 \text{ A} \end{array} \right\} L = 8.8 \text{ mH}.$$

Due to the autotransformer is saturated when the source voltage is increased, the winding connection used is not adequate for that application, and for that reason it is changed to parallel winding connection.

### B.2.2. Parallel Connection

The parallel connection of the machines is shown in Fig. B.10 and with this configuration the system can achieve the double of the power since the current is divided into the two branches.

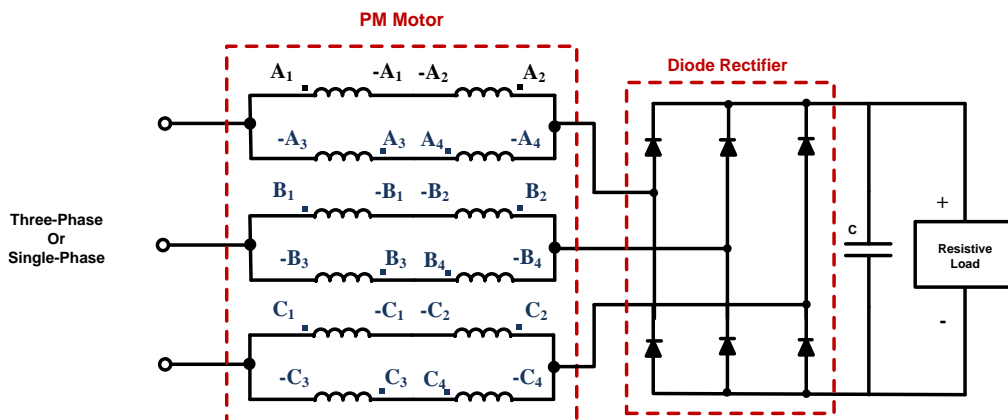


Figure B.10: Parallel winding connection for 20 kW PM motor.

The resistance, in this case and as it was commented before, was already known and has a value for this connection of:

$$R = 0.4 \Omega.$$

Since the voltage in the machine does not have a sinusoidal waveform (as can be observed in Fig. B.11), the inductance cannot be calculated by the previous method, because of that, for the calculation of the inductance, three phase voltage and current was recorded by the LECROY Wavepro 715 Oscilloscope and plotted by Matlab. The results obtain in Matlab are used for calculating the rms value of the voltage and current and with that values the inductance can be calculated.

The Matlab code is presenting and the waveforms of the three phase voltage and current are shown in Fig. B.11.

```
% Voltages and current for the 20 kW PM motor and calculations of the
% machine inductance
```

```
% Load of the data adquiered by the oscilloscope
```

```
load C1Trace00005.dat
load C2Trace00005.dat
load C3Trace00005.dat
load C4Trace00005.dat
```

```
% Current machine
```

```
x1=C1Trace00005(:,1);
y1=C1Trace00005(:,2);
```

```
% Phase A
```

```
x2=C2Trace00005(:,1);
y2=C2Trace00005(:,2);
```

```
% Phase B
```

```
x3=C3Trace00005(:,1);
y3=C3Trace00005(:,2);
```

```
% Voltage machine
```

```
x4=C4Trace00005(:,1);
y4=C4Trace00005(:,2);
```

```
subplot(2,1,1)
```

```
plot(x1,10*y1,'b',x2,y2,'g',x3,y3,'r',x4,5*y4,'k','linewidth',2)
```

```
xlabel('Time (s)','fontweight','b')
```

```
xlim([-0.02 0.02])
```

```
grid on
```

```
legend('iA (A*10)','V phase A','V phase B','V machine (V*5)')
```

```
subplot(2,1,2)
```

```
plot(x1,y1,'b',x4,y4,'k','linewidth',2)
```

```
xlabel('Time (s)','fontweight','b')
```

```
xlim([-0.02 0.02])
```

```
grid on
```

```
legend('iA (A)','V machine (V)')
```

```
Is=y1.*y1;
```

```
Vs=y4.*y4;
```

```
lv=length(x4); %Size of the vector
```

```
li=length(x1);
```

```
V_Int(1)=abs((x4(1)-0))*Vs(1); %The first integram term
```

```
I_Int(1)=abs((x1(1)-0))*Is(1);
```

```
for j=2:lv
```

```

V_Int(j)= V_Int(j-1)+(x4(j)-x4(j-1))*Vs(j); %Summation(Integral)
calculation
end

for i=2:li
    I_Int(i)= I_Int(i-1)+(x1(i)-x1(i-1))*Is(i);
end

Vrms=sqrt(1/(x4(li)-x4(1))*V_Int(li))
Irms=sqrt(1/(x1(li)-x1(1))*I_Int(li))

Re=0.4;
Wg=2*50*pi;

L=((Vrms/Irms)^2-Re^2)/Wg

```

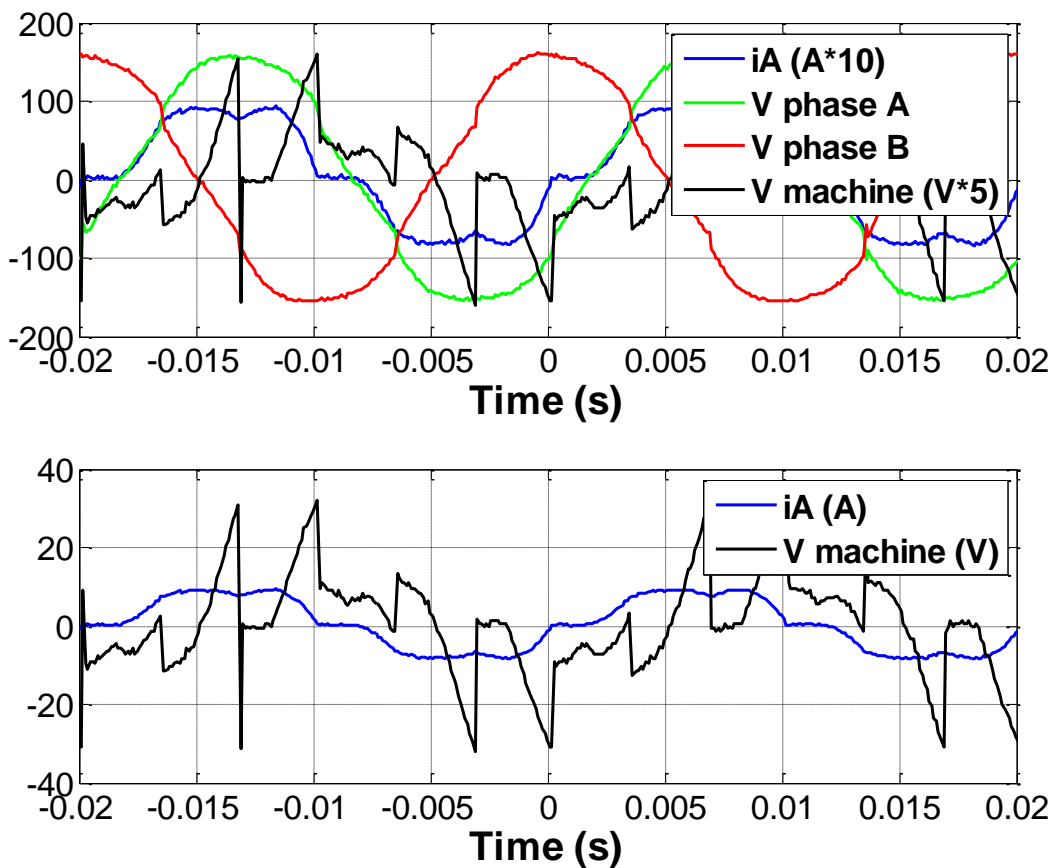


Figure B.11: Voltages and current in the experimental setup for the parallel winding connection.

The inductance calculated and the rms values of the voltage and the current are:

$$\left. \begin{array}{l} V = 12.7732 \text{ V} \\ I = 8.53 \text{ A} \end{array} \right\} L = 6.6 \text{ mH}.$$

During the test, the behavior against different position of the rotor was studied, and it was observed that rotating the rotor suppose changes in the value of the inductance. It is needed to comment also that during the test, the motor feed with high level of voltages start to be noisy.

Besides of this measurement, with this parallel configuration it is done a comparison between the experimental results and a simulation in Matlab/Simulink using Power System Blockset. The experimental value of the inductance is used in the simulated system. Fig. B.12 shows the simulation in Simulink and Fig. B.13 shows their results. In Fig. B.13 can be observed that the differences between both models are very small, being more appreciable in the case of the voltage. That can be explained by the fact of the voltage is the derivative of the current and this is a noisy operation, introducing harmonics in the current.

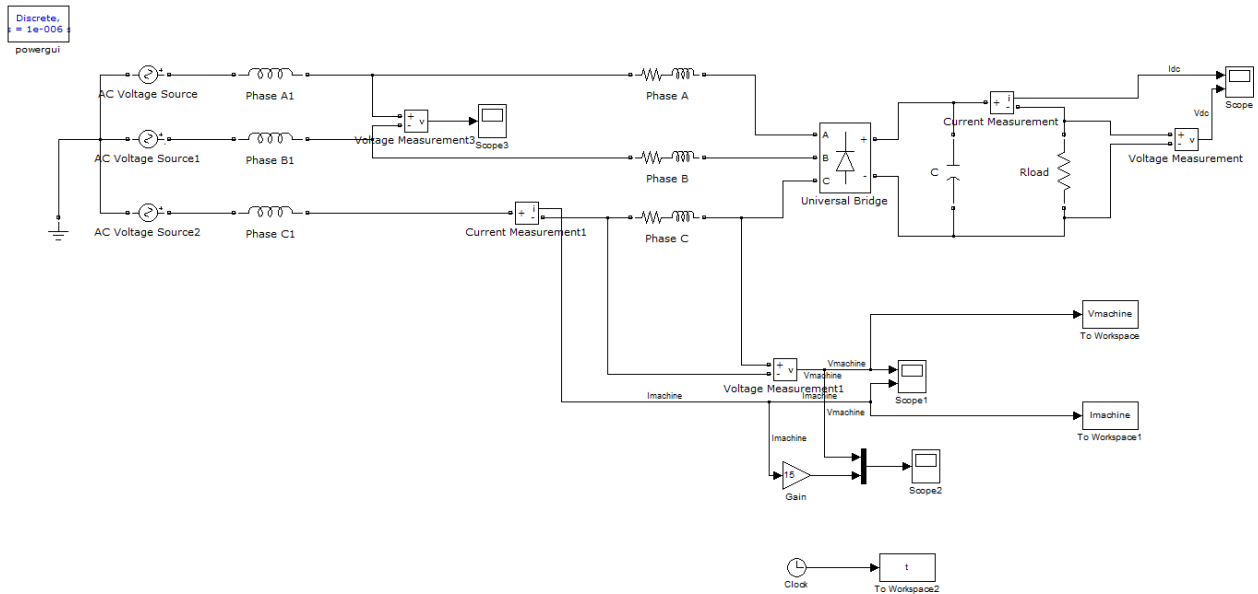


Figure B.12: Simulation of the integrated charger system studied.

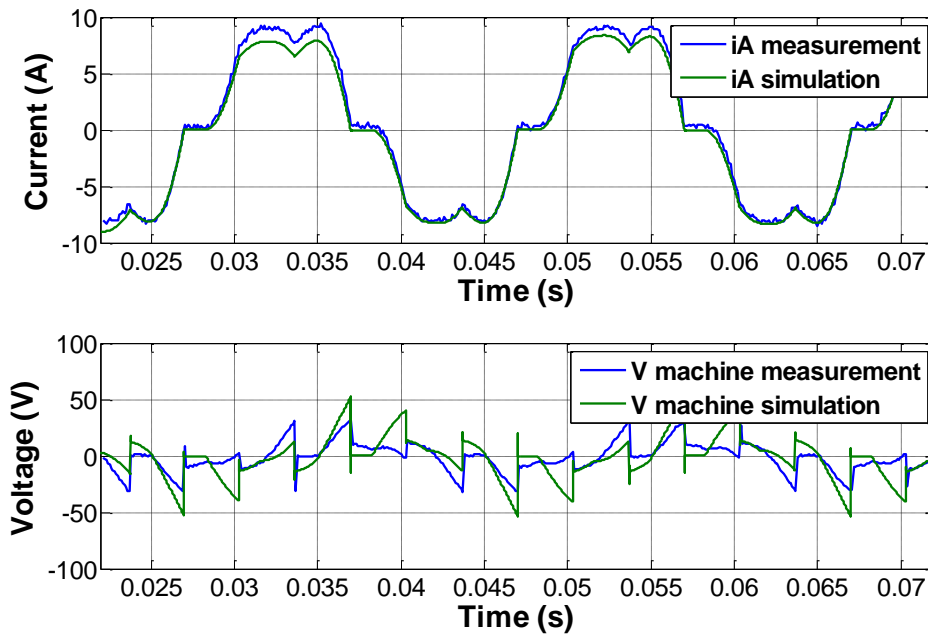


Figure B.13: Simulation results of the integrated charger system studied.

### B.3. Leakage Inductances

Since the value of the leakage inductance of the autotransformer and transformer, used in the experimental setup explain in Chapter 4, can affect to the results obtained in the experimental setup, different configurations are measured and the resulting inductance is calculated by equation (B.2).

$$L_{leak} = \frac{Z}{2\pi f} = \frac{U/I}{2\pi f} \quad (\text{B.2})$$

#### B.3.1. Transformer

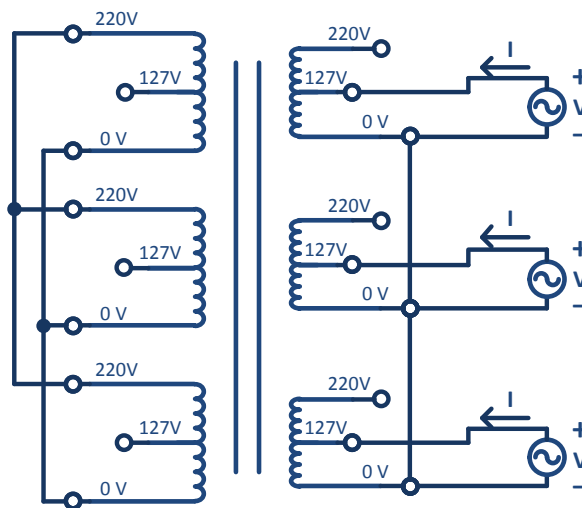


Figure B.14: Practical setup for measuring the leak inductance in the transformer.

Phase A	$V = 5,38 \text{ V}$ $I = 4,05 \text{ A}$	$L_{leak} = \frac{5,38/4,05}{2\pi 50} = 4,2284 \text{ mH}$	$L_{leak} = 4,237 \text{ mH}$
Phase B	$V = 5,38 \text{ V}$ $I = 4,04 \text{ A}$		
Phase C	$V = 5,36 \text{ V}$ $I = 4,02 \text{ A}$		

### B.3.2. Autotransformer

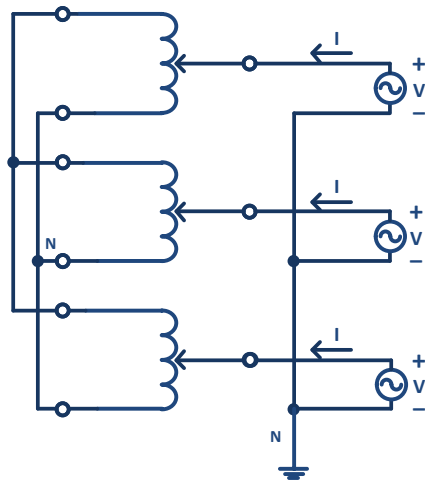


Figure B.15: Practical setup for measuring the leak inductance in the autotransformer.

Phase A	$V = 0,816 V$ $I = 6 A$	} $L_{leak} = \frac{0,816/6}{2\pi 50} = 0,4329 mH$	$L_{leak} = \mathbf{0,346 mH}$
Phase B	$V = 0,682 V$ $I = 6,7 A$		
Phase C	$V = 0,62 V$ $I = 7,02 A$		

### B.3.3. Autotransformer + Transformer

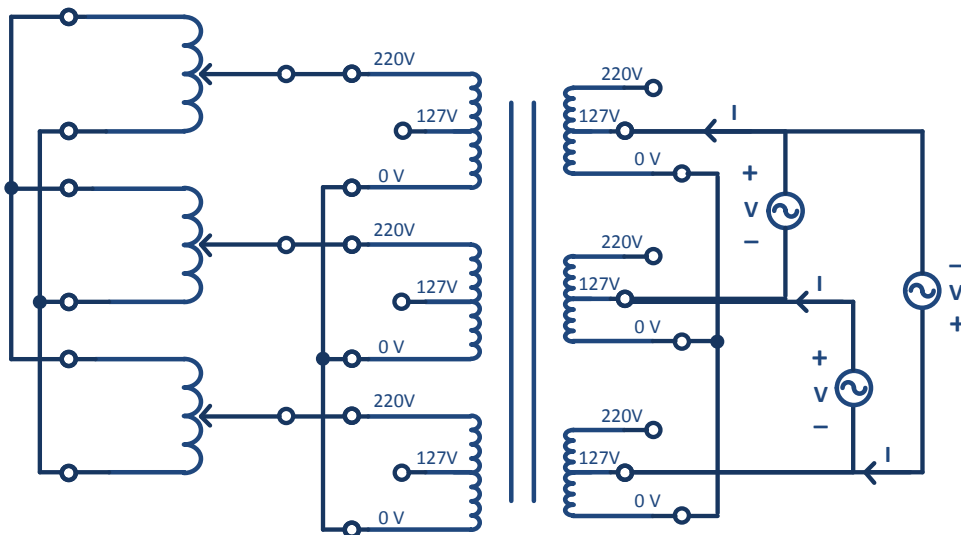


Figure B.16: Practical setup for measuring the leak inductance in the autotransformer+transformer.

$$\text{A-B} \quad \left. \begin{array}{l} V = 4,9 \text{ V} \\ I = 3,96 \text{ A} \end{array} \right\} L_{leak} = \frac{4,9/3,96}{2\pi 50} \frac{1}{2} = 1,9693 \text{ mH}$$

$$\text{B-C} \quad \left. \begin{array}{l} V = 4,93 \text{ V} \\ I = 3,99 \text{ A} \end{array} \right\} L_{leak} = \frac{4,93/3,99}{2\pi 50} \frac{1}{2} = 1,9665 \text{ mH} \quad \mathbf{L_{leak} = 1,9625 \text{ mH}}$$

$$\text{C-A} \quad \left. \begin{array}{l} V = 4,93 \text{ V} \\ I = 4,02 \text{ A} \end{array} \right\} L_{leak} = \frac{4,93/4,02}{2\pi 50} \frac{1}{2} = 1,9518 \text{ mH}$$



# Appendix C: Hardware Datasheets

## CompactRIO controller

### NI cRIO-9022

#### Real-Time Controller with 256 MB DRAM, 2 GB Storage

- Embedded controller runs LabVIEW Real-Time for deterministic control, data logging, and analysis
- 533 MHz processor, 2 GB nonvolatile storage, 256 MB DDR2 memory
- Dual Ethernet ports with embedded Web and file servers for remote user interface
- Hi-Speed USB host port for connection to USB flash and memory devices
- RS232 serial port for connection to peripherals; dual 9 to 35 VDC supply inputs
- -20 to 55 °C operating temperature range



Product Type	Controller (Computing Device)
Form Factor	CompactRIO
Part Number	780718-01
Operating System/Target	Real-Time
LabVIEW RT Support	Yes
CE Compliance	Yes
<b>Controller</b>	
Controller Type	High Performance
Processor Core Type	533 MHz PowerPC
CPU Clock Frequency	533 MHz
System Memory	256 MB
Legacy Product	No
Ethernet (# of ports)	2
Serial Ports (RS232)	1
USB Ports	Yes

Chassis	
Number of Slots	0
Integrated Controller	No
Input Voltage Range	9 V , 35 V
Recommended Power Supply: Power	55
Recommended Power Supply: Voltage	24
Power Consumption	35
Physical Specifications	
Length	77.3 mm
Width	90.2 mm
Height	88.1 mm
Weight	609 gram
Minimum Operating Temperature	-20 °C
Maximum Operating Temperature	55 °C
Maximum Altitude	2000 m

## CompactRIO analog input module NI 9215.

### 4 Ch, 100 kS/s, 16-Bit, $\pm 10$ V Simultaneous Sampling C Series Analog Input Module NI 9215



- 4 simultaneously sampled analog inputs, 100 kS/s
- -40 to 70 °C operating range
- NIST-traceable calibration
- Hot-swappable operation

#### Overview

The NI 9215 module for use with NI CompactDAQ and CompactRIO chassis includes four simultaneously sampled analog input channels and successive approximation register (SAR) 16-bit analog-to-digital converters (ADCs). The NI 9215 contains NIST-traceable calibration, a channel-to-earth ground double-isolation barrier for safety and noise immunity, and high common-mode voltage range.

#### Specifications Summary

General	
Product Name	NI 9215
Product Family	Industrial I/O
Form Factor	CompactDAQ , CompactRIO
Part Number	779011-01
Operating System/Target	Real-Time , Windows
Measurement Type	Voltage
Isolation Type	Ch-Earth Ground Isolation
RoHS Compliant	Yes
Analog Input	
Channels	4 , 0
Single-Ended Channels	0
Differential Channels	4
Resolution	16 bits
Sample Rate	100 kS/s
Max Voltage	10 V
Maximum Voltage Range	-10 V , 10 V
Maximum Voltage Range Accuracy	0.003 V
Simultaneous Sampling	Yes

<b>Analog Output</b>	
Channels	0
<b>Digital I/O</b>	
Bidirectional Channels	0
Input-Only Channels	0
Output-Only Channels	0
Number of Channels	0
<b>Counter/Timers</b>	
Counters	0
<b>Physical Specifications</b>	
Length	9 cm
Width	2.3 cm
I/O Connector	Screw terminals , BNC connectors
Minimum Operating Temperature	-40 °C
Maximum Operating Temperature	70 °C
Minimum Storage Temperature	-40 °C
Maximum Storage Temperature	85 °C
<b>Timing/Triggering/Synchronization</b>	
Triggers cDAQ Chassis	No

## CompactRIO digital input/output module NI 9401.

### NI 9401 Measurement System

#### 8 Ch, 5 V/TTL Bidirectional DIO for USB, Ethernet, and Wi-Fi

- Bundle includes measurement module and 1-slot NI CompactDAQ chassis
- USB, Ethernet, and 802.11 Wi-Fi connectivity
- 8-channel, 100 ns ultrahigh-speed digital I/O (DIO)
- Ability to access four general-purpose 32-bit counter/timers
- Industry-standard 25-pin D-SUB connector
- Bidirectional, configurable by nibble (4 bits)



#### Specifications Summary

General	
Product Name	NI 9401 Measurement Bundle
Product Family	Industrial I/O
Form Factor	USB , Wireless , CompactDAQ , Ethernet
Part Number	000000-00
Operating System/Target	Real-Time , Windows
Measurement Type	Digital
RoHS Compliant	Yes
Analog Input	
Channels	0
Single-Ended Channels	0
Differential Channels	0
Analog Output	
Channels	0
Digital I/O	
Bidirectional Channels	8
Input-Only Channels	0

Output-Only Channels	0
Number of Channels	0 , 8
Timing	Hardware
Max Clock Rate	10 MHz
Logic Levels	TTL
Supports Handshaking I/O?	Yes
Supports Pattern I/O?	Yes
Maximum Input Range	0 V , 5.25 V
Maximum Output Range	0 V , 5.25 V
<b>Counter/Timers</b>	
Counters	0
<b>Physical Specifications</b>	
Length	9 cm
Width	2.3 cm
I/O Connector	25-pin D-Sub
Minimum Operating Temperature	-40 °C
Maximum Operating Temperature	70 °C
Minimum Storage Temperature	-40 °C
Maximum Storage Temperature	85 °C
<b>Timing/Triggering/Synchronization</b>	
Triggering	Digital
Triggers cDAQ Chassis	Yes





1) The input circuit of the voltage transducer card, (VMT3), is designed in accordance to Fig 5. By omitting components and place a few straps, a circuit like Fig 2 can be achieved.

**AD210**

**INSIDE THE AD210**

The AD210 basic block diagram is illustrated in Figure 1. A +15 V supply is connected to the power port, and ±15 V isolated power is supplied to both the input and output ports via a 50 kHz carrier frequency. The uncommitted input amplifier can be used to supply gain or buffering of input signals to the AD210. The fullwave modulator translates the signal to the carrier frequency for application to transformer T1. The synchronous demodulator in the output port reconstructs the input signal. A 20 kHz, three-pole filter is employed to minimize output noise and ripple. Finally, an output buffer provides a low impedance output capable of driving a 2 kΩ load.

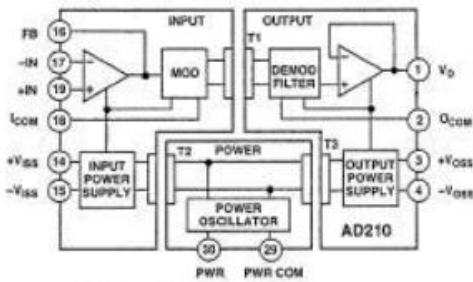


Figure 1. AD210 Block Diagram

**USING THE AD210**

The AD210 is very simple to apply in a wide range of applications. Powered by a single +15 V power supply, the AD210 will provide outstanding performance when used as an input or output isolator, in single and multichannel configurations.

**Input Configurations:** The basic unity gain configuration for signals up to ±10 V is shown in Figure 2. Additional input amplifier variations are shown in the following figures. For smaller signal levels Figure 3 shows how to obtain gain while maintaining a very high input impedance.

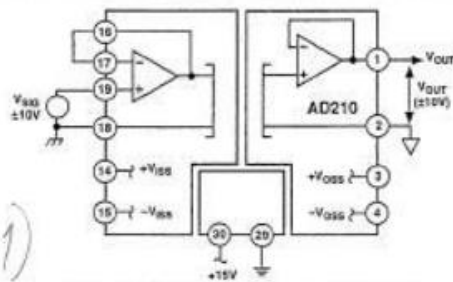


Figure 2. Basic Unity Gain Configuration

The high input impedance of the circuits in Figures 2 and 3 can be maintained in an inverting application. Since the AD210 is a three-port isolator, either the input leads or the output leads may be interchanged to create the signal inversion.

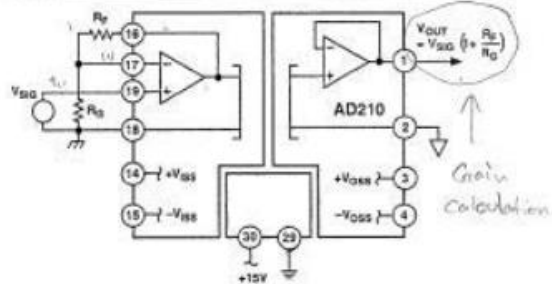


Figure 3. Input Configuration for  $G > 1$

Figure 4 shows how to accommodate current inputs or sum currents or voltages. This circuit configuration can also be used for signals greater than ±10 V. For example, a ±100 V input span can be handled with  $R_p = 20\text{ k}\Omega$  and  $R_{s1} = 200\text{ k}\Omega$ .

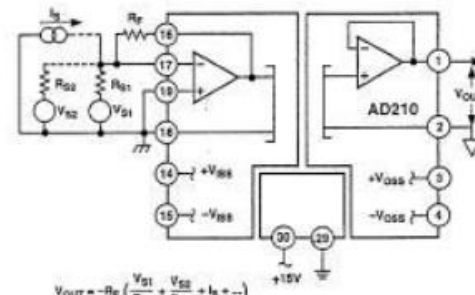


Figure 4. Summing or Current Input Configuration

**Adjustments**

When gain and offset adjustments are required, the actual circuit adjustment components will depend on the choice of input configuration and whether the adjustments are to be made at the isolator's input or output. Adjustments on the output side might be used when potentiometers on the input side would represent a hazard due to the presence of high common-mode voltage during adjustment. Offset adjustments are best done at the input side, as it is better to null the offset ahead of the gain.

Figure 5 shows the input adjustment circuit for use when the input amplifier is configured in the noninverting mode. This offset adjustment circuit injects a small voltage in series with the

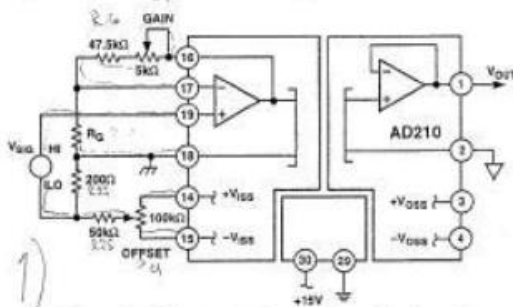


Figure 5. Adjustments for Noninverting Input

# AD210

low side of the signal source. This will not work if the source has another current path to input common or if current flows in the signal source LO lead. To minimize CMR degradation, keep the resistor in series with the input LO below a few hundred ohms.

Figure 5 also shows the preferred gain adjustment circuit. The circuit shows  $R_F$  of 50 k $\Omega$ , and will work for gains of ten or greater. The adjustment becomes less effective at lower gains (its effect is halved at  $G = 2$ ) so that the pot will have to be a larger fraction of the total  $R_F$  at low gain. At  $G = 1$  (follower) the gain cannot be adjusted downward without compromising input impedance; it is better to adjust gain at the signal source or after the output.

Figure 6 shows the input adjustment circuit for use when the input amplifier is configured in the inverting mode. The offset adjustment nulls the voltage at the summing node. This is preferable to current injection because it is less affected by subsequent gain adjustment. Gain adjustment is made in the feedback and will work for gains from 1 V/V to 100 V/V.

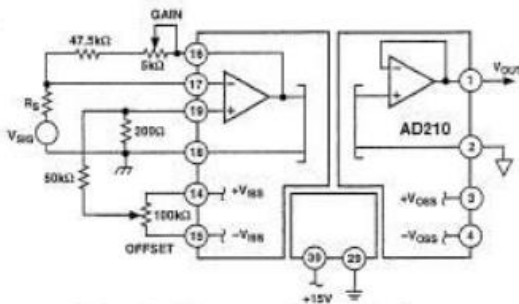


Figure 6. Adjustments for Inverting Input

Figure 7 shows how offset adjustments can be made at the output, by offsetting the floating output port. In this circuit,  $\pm 15$  V would be supplied by a separate source. The AD210's output amplifier is fixed at unity, therefore, output gain must be made ... a subsequent stage.

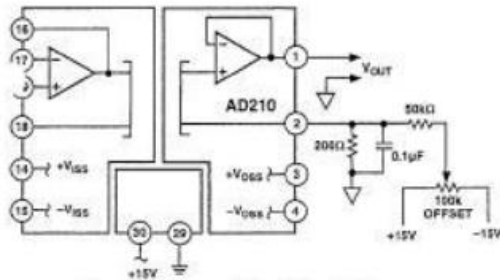


Figure 7. Output-Side Offset Adjustment

**PCB Layout for Multichannel Applications:** The unique pinout positioning minimizes board space constraints for multichannel applications. Figure 8 shows the recommended printed circuit board layout for a noninverting input configuration with gain.

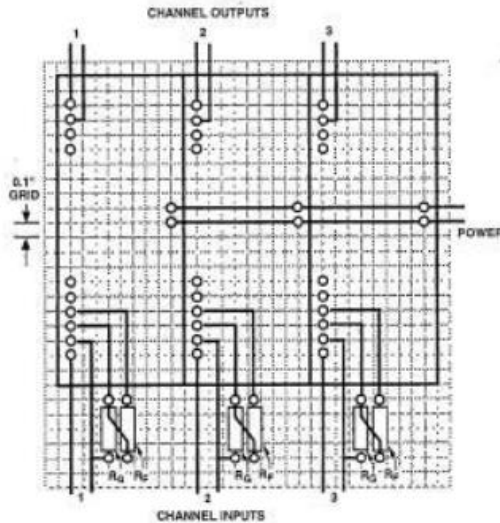


Figure 8. PCB Layout for Multichannel Applications with Gain

**Synchronization:** The AD210 is insensitive to the clock of an adjacent unit, eliminating the need to synchronize the clocks. However, in rare instances channel to channel pick-up may occur if input signal wires are bundled together. If this happens, shielded input cables are recommended.

### PERFORMANCE CHARACTERISTICS

**Common-Mode Rejection:** Figure 9 shows the common-mode rejection of the AD210 versus frequency, gain and input source resistance. For maximum common-mode rejection of unwanted signals, keep the input source resistance low and carefully lay out the input, avoiding excessive stray capacitance at the input terminals.

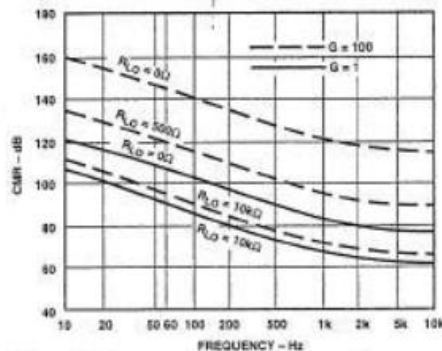


Figure 9. Common-Mode Rejection vs. Frequency

## LEM Current transducer



## Current Transducer LA 50-S/SP1

$$I_{PN} = 50 \text{ A}$$

For the electronic measurement of currents : DC, AC, pulsed..., with a galvanic isolation between the primary circuit (high power) and the secondary circuit (electronic circuit).



## Electrical data

$I_{PN}$	Primary nominal r.m.s. current	50	A
$I_P$	Primary current, measuring range	$0 \dots \pm 100$	A
$R_M$	Measuring resistance with $\pm 15 \text{ V}$		$R_{Mmin}$ $R_{Mmax}$
		@ $\pm 50 \text{ A}_{max}$	0 330 $\Omega$
		@ $\pm 100 \text{ A}_{max}$	0 100 $\Omega$
$I_{SN}$	Secondary nominal r.m.s. current	25	mA
$K_N$	Conversion ratio	1 : 2000	
$V_C$	Supply voltage ( $\pm 5 \%$ )	$\pm 15$	V
$I_C$	Current consumption	$10 + I_S$	mA
$V_d$	R.m.s. voltage for AC isolation test, 50 Hz, 1 min	3	kV

## Features

- Closed loop (compensated) current transducer using the Hall effect
- Insulated plastic case recognized according to UL 94-V0.

## Special features

- $I_P = 0 \dots \pm 100 \text{ A}$
- $K_N = 1 : 2000$

## Accuracy - Dynamic performance data

$X_a$	Overall accuracy @ $I_{PN}, T_A = 25^\circ\text{C}$	$\pm 0.5$	%
$\epsilon_L$	Linearity	$< 0.1$	%
$I_0$	Offset current @ $I_P = 0, T_A = 25^\circ\text{C}$	Typ $\pm 0.1$	mA
$I_{DT}$	Thermal drift of $I_0$ - $10^\circ\text{C} \dots +70^\circ\text{C}$	Max $\pm 0.4$	mA
$t_r$	Response time <sup>1)</sup> @ 90 % of $I_{PN}$	$< 1$	$\mu\text{s}$
$di/dt$	$di/dt$ accurately followed	$> 50$	A/ $\mu\text{s}$
$f$	Frequency bandwidth (-1 dB)	DC .. 150	kHz

## Advantages

- Excellent accuracy
- Very good linearity
- Low temperature drift
- Optimized response time
- Wide frequency bandwidth
- No insertion losses
- High immunity to external interference
- Current overload capability.

## General data

$T_A$	Ambient operating temperature	$-10 \dots +70$	$^\circ\text{C}$
$T_S$	Ambient storage temperature	$-25 \dots +85$	$^\circ\text{C}$
$R_s$	Secondary coil resistance @ $T_A = 70^\circ\text{C}$	130	$\Omega$
$m$	Mass Standards <sup>2)</sup>	45	g
		EN 50178	

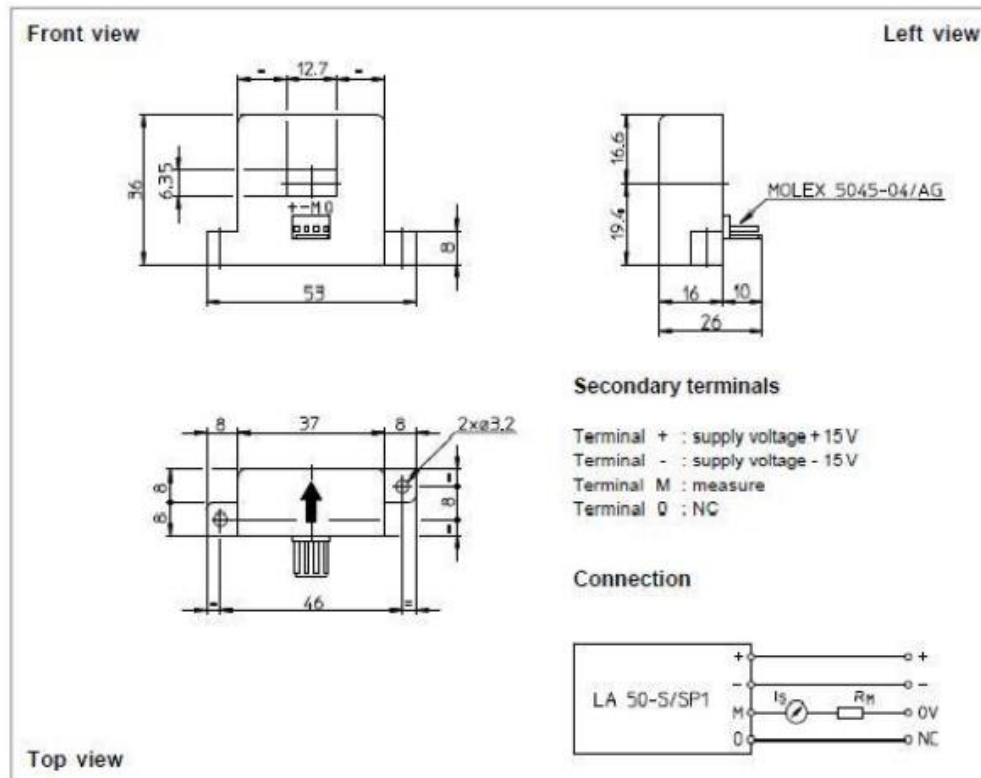
## Applications

- AC variable speed drives and servo motor drives
- Static converters for DC motor drives
- Battery supplied applications
- Uninterruptible Power Supplies (UPS)
- Switched Mode Power Supplies (SMPS)
- Power supplies for welding applications.

Notes : <sup>1)</sup> With a  $di/dt$  of 50 A/ $\mu\text{s}$

<sup>2)</sup> A list of corresponding tests is available.

991014/5


**Dimensions LA 50-S/SP1** (in mm. 1 mm = 0.0394 inch)

**Mechanical characteristics**

- General tolerance  $\pm 0.2$  mm
- Fastening 2 holes  $\varnothing 3.2$  mm
- Primary through-hole 12.7 x 6.35 mm
- Connection of secondary Molex 5045-04/AG

**Remarks**

- $I_s$  is positive when  $I_p$  flows in the direction of the arrow.
- Temperature of the primary conductor should not exceed 100°C.
- Dynamic performances (di/dt and response time) are best with a single bar completely filling the primary hole.
- In order to achieve the best magnetic coupling, the primary windings have to be wound over the top edge of the device.
- To measure nominal currents of less than 50 A, the optimum accuracy is obtained by having several primary turns (nominal current x number of turns < 50 At).

LEM reserves the right to carry out modifications on its transducers, in order to improve them, without previous notice.

## Semistack Semikron inverter

## SEMISTACK - IGBT

SEMITRANS Stack<sup>1)</sup>

Three-phase rectifier +  
inverter with brake  
chopper

SEMITEACH - IGBT  
SKM 50 GB 123D  
SKD 51  
P3/250F

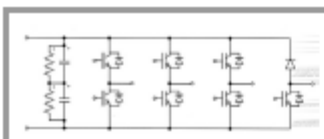
## Features

- Multi-function IGBT converter
- Transparent enclosure to allow visualization of every part
- IP2x protection to minimize safety hazards
- External banana/BNC type connectors for all devices
- Integrated drive unit offering short-circuit detection/cut-off, power supply failure detection, interlock of IGBTs + galvanic isolation of the user
- Forced-air cooled heatsink

## Typical Applications

- Education: One stack can simulate almost all existing industrial applications:
  - 3-phase inverter+brake chopper
  - Buck or boost converter
  - Single phase inverter
  - Single or 3-phase rectifier

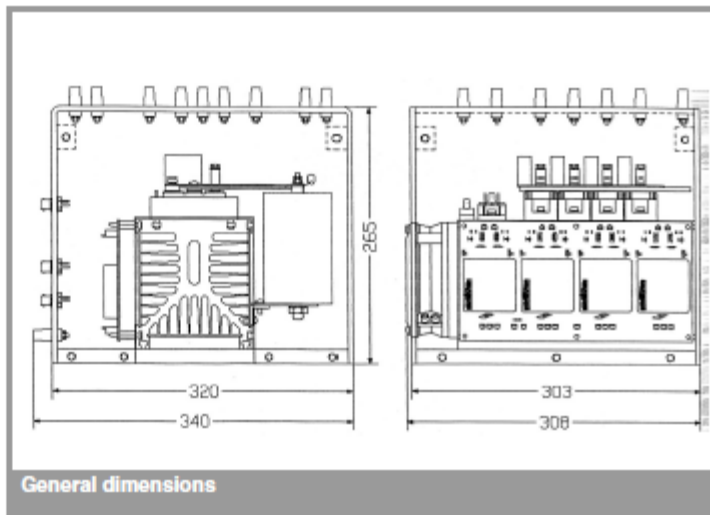
<sup>1)</sup> Photo non-contractual



B6CI + E1CIKF

Circuit	$I_{rms}$ (A)	$V_{ac} / V_{dcm\max}$	Types
B6CI	30	440 / 750	SEMITEACH - IGBT

Symbol	Conditions	Values	Units
$I_{rms}$	no overload IGBT - 4x SKM 50 GB 123D	30	A
$V_{CES}$	$I_c = 50A, V_{CE} = 15V, \text{chip level}; T_f = 25(125)^\circ C$	1200	V
$V_{CE(SAT)}$		2,7 (3,5)	V
$V_{GES}$		$\pm 20$	V
$I_c$	$T_{case} = 25 (80)^\circ C$	50 (40)	A
$I_{CM}$	$T_{case} = 25 (80)^\circ C; t_p = 1ms$	100 (80)	A
$V_{in(max)}$	Rectifier - 1x SKD 51/14		
	without filter with filter	3 x 480 3 x 380	V V
$C_{dqf}$ $V_{DCmax}$	DC Capacitor bank - Electrolytic 2x 2200 $\mu F$ /400V	1100 / 800	$\mu F / V$
	total equivalent capacitance max. DC voltage applied to the capacitor bank	750	V
Power supply	Driver - 4x SKHI 22	0 / 15	V
Current consumption	max; per driver	16	mA
Thermal trip	Normally Open type (NO)	71	$^\circ C$



General dimensions

This technical information specifies semiconductor devices but promises no characteristics. No warranty or guarantee expressed or implied is made regarding delivery, performance or suitability.